Arabian Journal of Chemistry (2022) **15**, 103532

King Saud University

Arabian Journal of Chemistry

www.ksu.edu.sa
www.sciencedirect.com

ORIGINAL ARTICLE

Antimycobacterial and anticancer activity of newly designed cinnamic acid hydrazides with favorable toxicity profile

Mohamed H. Assaleh [a,b], Snezana K. Bjelogrlic [c], Nevena Prlainovic [a], Ilija Cvijetic [d], Aleksandra Bozic [e], Irena Arandjelovic [f], Dragana Vukovic [f], Aleksandar Marinkovic [a,*]

[a] *Faculty of Technology and Metallurgy, University of Belgrade, Karnegijeva 4, 11000 Belgrade, Serbia*
[b] *CID Forensics Laboratory, Toxicology Unit Lab, Tripoli, Libya*
[c] *National Cancer Research Center, Pasterova 14, Belgrade, Serbia*
[d] *Faculty of Chemistry, University of Belgrade, Studentski trg 12-16, 11000 Belgrade, Serbia*
[e] *Academy of Applied Technical Studies, Katarine Ambrozic 3, Belgrade, Serbia*
[f] *Institute of Microbiology and Immunology, Faculty of Medicine, University of Belgrade, Dr. Subotica 1, Serbia*

Received 20 August 2021; accepted 27 October 2021
Available online 30 October 2021

KEYWORDS

Cinnamic acid hydrazides;
Mycobacterium tuberculosis;
Anti-mycobacterial;
Anti-cancer;
Hepatotoxicity

Abstract A series of twelve novel hybrids of cinnamic acid and thiocarbohydrazones were designed, synthesized in high yield using a simple coupling strategy *via* acid chlorides, and evaluated for their impact against *Mycobacterium tuberculosis* (*Mtb*) and cancer cells survival. Among them, compound **3** demonstrated strong anti-*Mtb* activity by reducing bacilli survival for > 90 % in all three treated *Mtb* isolates, whereas isoniazid and rifampicin did not. Moreover, compound **3** didn't affect vitality of HepG-2 cells, implying on advantageous hepatotoxicity profile compared to current therapeutic options for tuberculosis. Compounds **2a** and **3b** displayed as strong inducers of apoptosis in A549 cells, both activating intrinsic caspase pathway and cell cycle arrest at the G0/G1 phase. Subsequent analyses disclosed differences in their activities, where **3b** has ability to induce production of mitochondrial superoxide anions, while **2a** significantly inhibited cellular mobility. More importantly, **3b** considerably affected viability of HepG-2 and HaCaT cells, whereas **2a** had moderate impact only on the later. Molecular modeling studies indicated high permeability and good absorption through the human intestine, and moderate aqueous solubility with poor blood–brain barrier permeability. In summary, our results reveal that novel compounds **3** and **2a**

* Corresponding author.
E-mail address: marinko@tmf.bg.ac.rs (A. Marinkovic).
Peer review under responsibility of King Saud University.

Production and hosting by Elsevier

https://doi.org/10.1016/j.arabjc.2021.103532

represent promising agents for tuberculosis and cancer treatment, respectively, indicating that further investigation needs to be performed to clarify the mechanisms of their anti-*Mtb* and anticancer activity.

1. Introduction

Mycobacterium tuberculosis (*Mtb*) is a pathogen responsible for development of tuberculosis (TB), which has long been the deadliest infectious disease worldwide. Globally, 10 million people developed TB in 2019, with the annual number of TB deaths estimated at 1.4 million (World Health Organization, 2021). While SARS-CoV-2 overtook *Mtb* as the infectious agent killing the most people per day in 2020, the COVID-19 pandemic is expected to further increase TB death rates (Glaziou, 2020). Isoniazid (INH) and rifampicin (RIF) are two most important drugs in the first-line treatment of TB. However, continual emergence of *Mtb* strains resistant to INH and/or RIF presents a great threat to the global TB control, as currently available drugs for INH- and RIF-resistant strains are less effective, more expensive and more toxic. Malignancies, on the other hand, as non-communicable diseases are responsible for twice as many deaths as cardiovascular diseases in high-income countries (Dagenais et al., 2020). Despite notable advances in clinical and molecular diagnosis, innovative approaches in chemotherapy and targeted therapy, there were 24.5 million newly diagnosed cancer patients and 9.6 million cancer deaths worldwide in 2017 (Global Burden of Disease Cancer Collaboration, 2019). Therefore, at the beginning of the third millennium, cancer and TB research are still aimed at the discovery of new drugs and therapeutic strategies that would provide more efficient treatments with less adverse effects compared to the currently available regimens.

The rational of the current investigation was to create a set of new small molecules by hybridization of two pharmacophores that were previously tested for anticancer and/or anti-*Mtb* activities. A thorough screening of the compound libraries available and published data led to selection of cinnamic acid and thiocarbohydrazones (TCHs) as preferable scaffolds according to reactive groups in each pharmacophore, and the bond type their hybridization would create in the final structure. Cinnamic acid is an aromatic fatty acid composed of a phenyl ring substituted with an acrylic acid group that is usually found as *trans*-isomer. It is greatly abundant in nature, occurring in plants usually in form of esters with other acids, lipids or sugars, or in form of amides with aromatic and aliphatic amines (Shuab et al., 2016). In medicinal chemistry, cinnamoyl scaffold is a privileged and important pharmacophore considering its derivatives are known for antioxidant (Sova, 2012), anticancer (De, Prithwiraj et al., 2011a; Luo et al., 2015; Pontiki et al., 2014; Sankara Rao et al., 2019; Zhu et al., 2016), antimalarial (Teixeira et al., 2014), antimicrobial (Guzman, 2014), and antitubercular (De, Prithwiraj et al., 2011b; De et al., 2012; Kakwani et al., 2011; Teixeira et al., 2020) properties. Additionally, its α,β-unsaturated carbonyl moiety can be considered as a Michael acceptor that is frequently employed in design of anticancer drugs.

Thiosemicarbazones (TSCs) have been the focus of interest of anticancer and antimicrobial drug research groups since the middle of the previous century (Heffeter et al., 2018). The first drug of this chemical class used in human medicine is *p*-acetamidobenzaldehyde TSC (Thiacetazone, Fig. 1), that up to recently had been employed for the treatment of INH-resistant TB, but was withdrawn due to serious side effects (Alahari et al., 2007; Miller et al., 1966; Nunn et al., 1993). Anticancer clinical studies on 5-hydroxyl-2-formylpyridine TSC (5-HP, Fig. 1) and 3-aminopyridine-2-carboxaldehyde TSC (3-AP, Fig. 1) have been canceled, because 5-HP was revealed as highly toxic (DeConti et al., 1972), while 3-AP displayed poor pharmacokinetic properties with therapeutic abilities limited to hematologic malignancies (Chao et al., 2012; Feun et al., 2002; Ma et al., 2008; Yen et al., 2004). Therefore, in recent years attention from TSCs has been shifted toward their higher homologues - TCHs (Bonaccorso et al., 2019). Our previous experience with TCHs showed them as potent pro-apoptotic agents in human malignant cell models (Bozic et al., 2016), while the others reported on moderate activity of symmetric TCH derivatives against *Mycobacterium bovis* associated with low toxicity profile (Tehrani et al., 2013). An additional stimulus to select TCHs as favorable pharmacophore for hybridization with cinnamoyl scaffold was the fact that INH is pyridine-4-carbohydrazide (Fernandes et al., 2017). Therefore, we hypothesized that carbohydrazides resulting from reaction between carboxylic group of cinnamic acid and free amino group in TCHs may have promising anti-*Mtb* activity due to structural similarity with INH (Fig. 1). Since the previous research of antimicrobial activity of TCHs having 2-, 3- and 4-pyridine rings (Bozic et al., 2018) demonstrated that only 2-pyridine derivatives showed antimicrobial

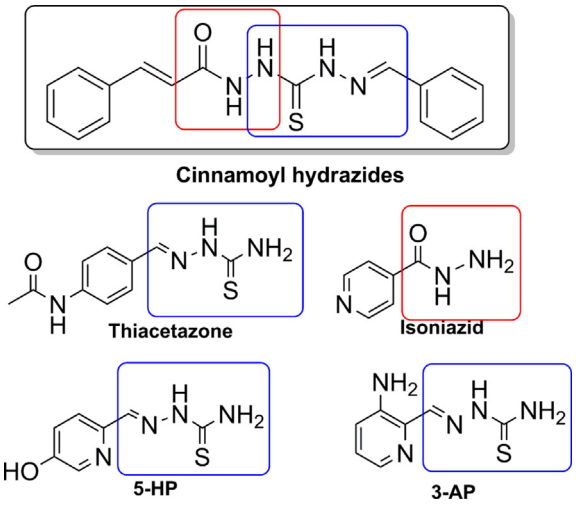

Fig. 1 Structural similarity between cinnamic acid hydrazides and several anti-*Mtb* and anticancer agents.

potential, 3- and 4-pyridine structures were not considered further. On the other hand, heterocyclic amides of cinnamic acid are well known for the broad spectrum of biological activities, including anticancer and anti-*Mtb* effects (Gaikwad et al., 2019).

In the current manuscript we represent design, synthesis, structural and biological characterization of twelve new cinnamic hydrazides whose anticancer and anti-*Mtb* activity have been tested, as well as their toxicity profiles in two *in vitro* models. Molecular modeling study was combined with the experimental data to suggest possible molecular targets and relevant biological pathways.

2. Experimental

2.1. Chemicals

Cinnamic acid, 3-chlorocinnamic acid, 4-chlorocinnamic acid, and thionyl chloride were obtained from Fluka AG - Chemische. 2-Formylpyridine, salicylaldehyde, and 2-acetylpyridine were purchased from Sigma-Aldrich. Methanol, ethanol, dimethylformamide (DMF), ethyl acetate, and hexane were obtained from Fisher Chemical, while 8-hydroxy-2-quinoline carboxaldehyde was supplied by Acros. All chemicals and reagents were of commercial quality and used without further purification.

2.2. Instruments

Melting points (mp) were determined on an SMP30 - Digital melting point apparatus. Elemental analyses (C, H, N) were performed by the standard micromethods using the ELEMENTAR Vario ELIII C.H.N.S = O analyzer.

Attenuated total reflectance (ATR) infrared (IR) spectra were obtained by Nicolet iS10 FTIR (Thermo Scientific USA) spectrometer with Smart iTX™ accessory. Infrared (IR) spectra were recorded on a Thermo Scientific™ Nicolet™ iS1010 spectrometer.

NMR spectroscopy was performed on a Bruker Avance III 500 spectrometer equipped with a broad-band direct probe. The spectra were recorded at room temperature in DMSO d_6. Chemical shifts are given on δ scale relative to tetramethylsilane (TMS) as internal standard for ^{1}H and ^{13}C. Coupling constants (J) were expressed in Hz. Abbreviations used for NMR spectra: s (singlet), d (doublet), dd (doublet of doublets), t (triplet), m (multiplet) and br. m. ovlp. (broad multiplet overlapping). 1D (^{1}H and ^{13}C) and 2D (COSY, NOESY, ^{1}H–^{13}C HSQC and ^{1}H–^{13}C HMBC) spectra of all compounds are shown in Electronic Supplementary Information (ESI), Figures S1–S35.

2.3. General procedure for the synthesis of cinnamic acid hydrazides ***1-4b***

The synthesis of twelve new compounds is shown in Fig. 2. The first step was synthesis of chlorides of cinnamic acid or its analogues according to the procedure described previously (Dias et al., 2017; Kumari et al., 2016; Shi et al., 2014). Briefly, cinnamic acid or its analogue (0.9 mmol) was added into a huge excess of thionyl chloride (30 eq., 27 mmol). The mixture was allowed to stir under reflux for 5 h, and then distilled under vacuum to remove excess thionyl chloride. The rest was washed with DMF and used without further purification. In the next step, to a previously obtained cinnamoyl chlorides, a solution of synthesized monothiocarbohydrazones (MTCHs, **M1-M4**, 0.82 mmol, Fig. 2) in DMF (2 mL) was added dropwise. MTCHs **M1-M4** were prepared according to the previously published procedure (Bozic et al., 2016). The mixture was heated at 40 ℃ and stirred for 24 h. After that the solution was filtrated and 20 mL of water was added to the filtrate and left for an hour to precipitate. Next, the solution was filtrated again and the obtained products were purified by recrystallization from methanol or ethyl acetate.

The composition and purity of all compounds were verified by elemental analysis, and the structure was assigned using IR and NMR spectroscopy.

2.4. Characterization

N'-((E)-2-(pyridin-2-ylmethylene)hydrazinecarbonothioyl)cinnamohydrazide (1)

The compound was obtained as a white powder (69% yield), mp 205–206 ℃. Anal: $C_{16}H_{15}N_5OS$ (Mw = 325.10 g mol^{-1}): Calculated: C, 59.06; H, 4.65; N, 21.52; S, 9.85%; Found: C, 59.01; H, 4.59; N, 21.46; S, 9.78 %. IR-ATR (cm^{-1}): C = S (1283.80), C = N (1628.54), C = O (1673.25), NH (3180.70), NH amide (3250.17). ^{1}H NMR (400 MHz, DMSO d_6, δ (ppm)): 12.04 (*s*, H-N$_2$, 1H), 10.47 (*s*, H-N$_3$, 1H), 10.30 (*s*, H-N$_4$, 1H), 8.60 (*d*, H–C$_6$, $^3J_{6,5}$ = 4.3 Hz 1H), 8.40 (*d*, H-C$_3$, $^3J_{3,4}$ = 8.0 Hz, 1H), 8.15 (*s*, H-C$_7$, 1H), 7.87 (*td*, H-C$_4$, $^3J_{4,3}$ = 7.8 Hz, $^3J_{4,5}$ = 1.2 Hz, 1H), 7.64 (*d*, H-C$_{13}$ = H-C$_{17}$, $^3J_{13,14}$ = $^3J_{17,16}$ = 6.7 Hz, 2H), 7.59 (*d*, H-C$_{11}$, $^3J_{11,10}$ = 15.9 Hz, 1H), 7.48 – 7.37 (*m*, H-C$_{14}$ = H-C$_{16}$, H-C$_{15}$, H-C$_5$, 4H), 6.78 (*d*, H-C$_{10}$, $^3J_{10,11}$ = 15.9 Hz, 1H). ^{13}C NMR (101 MHz, DMSO d_6, δ (ppm)): 179.26 (C$_8$), 164.60 (C$_9$), 153.65 (C$_2$), 149.84 (C$_6$), 143.99 (C$_7$), 140.69 (C$_{11}$), 136.98 (C$_4$), 135.08 (C$_{12}$), 130.30 (C$_{14}$ = C$_{16}$), 129.49 (C$_{15}$), 128.18 (C$_{13}$ = C$_{17}$), 124.73 (C$_5$), 120.93 (C$_3$), 120.11 (C$_{10}$).

N'-((E)-2-(2-hydroxybenzylidene)hydrazinecarbonothioyl)cinnamohydrazide (2)

The compound was obtained as a white powder (86% yield), mp 197–200 ℃. Anal: $C_{17}H_{16}N_4O_2S$ (Mw = 340.10 g mol^{-1}): Calculated: C, 59.98; H, 4.74; N, 16.46; S, 9.42 %; Found: C, 53.33; H, 3.80; N, 19.35; S, 8.79 %. IR-ATR (cm^{-1}): C = S (1276.27), C = N (1628.56), C = O (1667.33), NH (3257.87), NH amide (3333.85). ^{1}H NMR (400 MHz, DMSO d_6, δ (ppm)): 11.77 (*s*, H-N$_2$, 1H), 10.25 (*s*, H-N$_3$, C-OH, 2H), 9.93 (*s*, H-N$_4$, 1H), 8.44(*s*, H-C$_7$, 1H), 8.05 (*d*, H–C$_6$, $^3J_{6,5}$ = 5.6 Hz, 1H), 7.63 (d, H-C$_{17}$ = H-C$_{13}$, $^3J_{13,14}$ = $^3J_{17,16}$ = 7.1 Hz, 2H), 7.58 (*d*, 1H, H-C$_{11}$, $^3J_{11,10}$ = 15.9 Hz), 7.49 – 7.38 (*m*, H-C$_{15}$, H-C$_{14}$ = H-C$_{16}$, 3H), 7,25 (*t*, H–C$_4$, J = 7.6 Hz, 1H,), 6,90 (*d*, H–C3, $^3J_{3,4}$ = 8.2 Hz, 1H), 6,85 (*t*, H–C$_5$, J = 7.5 Hz, 1H), 6.78 (*d*, H-C$_{10}$, $^3J_{10,11}$ = 15.8 Hz, 1H,). ^{13}C NMR (101 MHz, DMSO d_6, δ (ppm)): 178.66 (C$_8$), 164.55 (C$_9$), 157.06 (C$_1$), 140.55 (C$_7$), 135.09 (C$_{11}$), 131.78 (C$_{12}$), 130.28 (C$_5$), 129.50 (C$_{15}$), 128.24 (C$_{14}$ = C$_{16}$), 128.16 (C$_{13}$ = C$_{17}$), 127.47 (C$_3$), 120.67 (C$_{10}$), 120.19 (C$_6$), 119.69 (C$_4$), 116.60 (C$_2$).

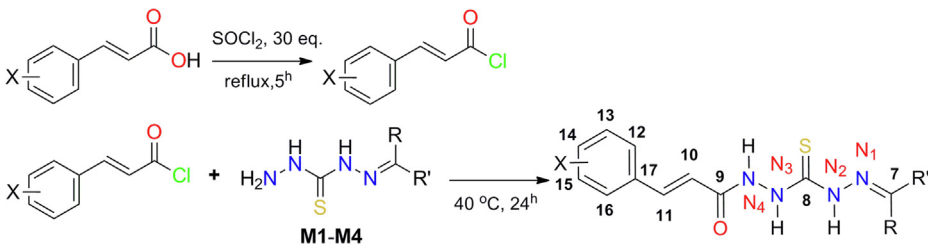

Compound	X	R	R'
1,1a,1b	1=H, 1a=*m*-Cl 1b=*p*-Cl	H	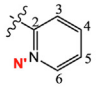
2, 2a, 2b	2=H, 2a=*m*-Cl 2b=*p*-Cl	H	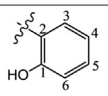
3, 3a, 3b	3=H, 3a=*m*-Cl 3b=*p*-Cl	H	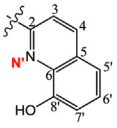
4, 4a, 4b	4=H, 4a=*m*-Cl 4b=*p*-Cl	CH_3	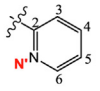

Fig. 2 General procedure for the synthesis of cinnamic acid hydrazides **1-4b**, along with the atom numbering scheme.

N'-((E)-2-((8-hydroxyquinolin-2-yl)methylene)hydrazinecarbonothioyl)cinnamohydrazide (3)

The compound was obtained as a very slight yellow powder (88% yield), mp 204–206 ℃. Anal $C_{20}H_{17}N_5O_2S$ (*Mw* = 391.11 g mol^{-1}): Calculated: C, 61.37; H, 4.38; N, 17.89; S, 8.19%; Found: C, 61.30; H, 4.29; N, 17.79; S, 8.11%. IR-ATR (cm^{-1}): C = S (1270.12), C = N (1629.74), C = O (1668.25), NH (3166.72), NH amide (3298.26). ^{1}H NMR (400 MHz, DMSO d_6, δ (ppm)): 12.30 (*s*, H-N_2, 1H), 10.63 (*s*, H-N_3, 1H), 10.38 (*s*, H-N_4, 1H), 9.94 (*s*, OH, 1H), 8.56 (*d*, H–C_3, $^3J_{3,4}$ = 8,7 Hz, 1H), 8.33 (*d*, H–C_4, H–C_7, *J* = 7.7 Hz, 2H), 7.66 (*d*, H-C_{13} = H-C_{17}, $^3J_{13,14}$ = $^3J_{17,16}$ = 7.2 Hz, 2H), 7.61 (*d*, H-C_{11}, $^3J_{11,10}$ = 15.9 Hz, 1H), 7.49 – 7.38 (*m*, H-C_{14} = H-C_{16}, H-C_{15}, H-$C_{5'}$, H-$C_{6'}$, 5H), 7.12 (*d*, H–$C_{7'}$, $^3J_{7',6'}$ = 7,4 Hz, 1H), 6.80 (*d*, H-C_{10}, $^3J_{10,11}$ = 15.9 Hz, 1H). ^{13}C NMR (101 MHz, DMSO d_6, δ (ppm)): 179.32 (C_8), 164.67 (C_9), 153.97 ($C_{8'}$), 152.12 (C_2), 143.85 (C_7), 140.76 (C_{11}), 138.68 (C_6), 136.64 (C_4), 135.03 (C_{12}), 130.35 (C_{14} = C_{16}), 129.52 (C_{15}), 129.34 ($C_{6'}$), 128.70 (C_5), 128.21 (C_{13} = C_{17}), 120.03 (C_{10}), 119.08 (C_3), 118.23 ($C_{5'}$), 112.64 ($C_{7'}$).

N'-((E)-2-(1-(pyridin-2-yl)ethylidene)hydrazinecarbonothioyl)cinnamohydrazide (4)

The compound was obtained as a white powder (79 % yield), mp 170–173 ℃. Anal: $C_{17}H_{17}N_5OS$ (*Mw* = 339.12 g mol^{-1}): Calculated: C, 60.16; H, 5.05; N, 20.63; S, 9.45%; Found: C, 60.06; H, 4.98; N, 20.53; S, 9.35%. IR-ATR (cm^{-1}): C = S (1205.48), C = N (1615.58), C = O (1668.84), NH(3174.88), NH amide (3300.70). ^{1}H NMR (400 MHz, DMSO d_6, δ (ppm)): 10.80 (*s*, H-N_2, 1H), 10.30–10.42 (*br.m.ovlp.*, H-N_3, H-N_4, 2H), 8.61 (*dd*, H–C_6, $^3J_{6,5}$ = 4.8 Hz, $^3J_{6,4}$ = 0.7 Hz, 1H), 8.56 (*d*, H-C_3, $^3J_{3,4}$ = 8.1 Hz, 1H), 7.83 (*td*, H-C_4, $^3J_{4,3}$ = 8.1 Hz, $J_{4,5}$ = 1.7 Hz, 1H), 7.64 (*d*, H-C_{13} = H-C_{17}, $^3J_{13,14}$ = $^3J_{17,16}$ = 6.7 Hz, 2H), 7.59 (*d*, H-C_{11}, $^3J_{11,10}$ = 15.9 Hz, 1H), 7.47 – 7.39 (*m*, H-C_{14} = H-C_{16}, H-C_{15}, H-C_5, 4H), 6.80 (*d*, H-C_{10}, $^3J_{10,11}$ = 15.9 Hz, 1H), 2.44 (s, H-C_{methyl}, 3H). ^{13}C NMR (101 MHz, DMSO d_6, δ (ppm)): 179.70 (C_8), 164.44 (C_9), 154.96 (C_2), 148.96 (C_6), 144.39 (C_7), 140.66 (C_{11}), 136.79 (C_4), 130.31 (C_{15}), 129.51 (C_{14} = C_{16}), 128.66 (C_{12}), 128.18 (C_{13} = C_{17}), 124.59 (C_5), 121.65 (C_3), 120.22 (C_{10}), 12.531(C_{methyl}).

(E)-3-(3-chlorophenyl)-N'-((E)-2-(pyridin-2-ylmethylene)hydrazinecarbonothioyl)acrylohydrazide (1a)

The compound was obtained as a beige powder (72% yield), mp 212–215 ℃. Anal: $C_{16}H_{14}ClN_5OS$ (*Mw* = 359.06 g mol^{-1}): Calculated: C, 53.41; H, 3.92; N, 19.46; S, 8.91%; Found: C, 53.39; H, 3.88; N, 19.40; S, 8.85%. IR-ATR (cm^{-1}): C = S (1289.58), C = N (1631.97), C = O (1677.01), NH (3177.54), NH amide (3253.67). ^{1}H NMR (400 MHz, DMSO d_6, δ (ppm)): 12.10 (s, H-N_2, 1H), 10.52 (s, H-N_3, 1H), 10.35 (s, H-N_4, 1H), 8.59 (d, H–C_6, $^3J_{6,5}$ = 4.6 Hz, 1H), 8.41 (d, H-C_3, $J_{3,4}$ = 7.8 Hz, 1H), 8.14 (s, H-C_7, 1H), 7.86 (t, H-C_4, $^3J_{4,3}$ = 7.8 Hz, 1H), 7.73 (s, H-C_{17}, 1H), 7.65 – 7.61 (m, H-C_{14}, 1H), 7.58 (d, H-C_{11}, $^3J_{11,10}$ = 15.9 Hz, 1H), 7.49 (d, H-C_{13}, H-C_{15}, $^3J_{13,14}$ = $^3J_{15,14}$ = 4.5 Hz, 2H), 7,41 (m, H–C_5, 1H), 6.83 (d, H-C_{10}, $^3J_{10,11}$ = 15.9 Hz, 1H). ^{13}C NMR (101 MHz, DMSO d_6, δ (ppm)): 179.20 (C_8), 164.29 (C_9), 153.61 (C_2), 149.86 (C_6), 144.02 (C_7), 139.21 (C_{11}), 137.33 (C_{12}), 137.01 (C_4), 134.22

(C_{16}), 131.33 (C_{15}), 129.95 (C_{13}), 127.99 (C_{17}), 126.58 (C_{14}), 124.77 (C_5), 121.72 (C_{10}), 120.93 (C_3).

(E)-3-(3-chlorophenyl)-N'-((E)-2-(2-hydroxybenzylidene)hydrazinecarbonothioyl)acrylohydrazide (2a)

The compound was obtained as a beige powder (79% yield), mp 191–194 ℃. Anal: $C_{17}H_{15}ClN_4O_2S$ (Mw = 374.06 g mol^{-1}): Calculated: C, 54.47; H, 4.03; N, 14.95; S, 8.55%; Found: C, 54.38; H, 3.98; N, 14.87; S, 8.50%. IR-ATR (cm^{-1}): C = S (1267.48), C = N (1632.39), C = O (1670.34), NH(3182.42), NH amide (3345.63). ^{1}H NMR (400 MHz, DMSO d_6, δ (ppm)): 11.80 (*s*, H-N_2, 1H), 10.27 (*s*, H-N_3, C_1-OH, 2H), 9.95 (*s*, H-N_4, 1H), 8.44 (*s*, H-C_7, 1H), 8.06 (d, H–C_6, $^3J_{6,5}$ = 6.1 Hz, 1H), 7.71 (s, H-$C_{17,}$ 1H), 7.61 (dd, H-$C_{14,}$ J = 4.9 Hz, 1H), 7.57 (d, H-C_{11}, $^3J_{11,10}$ = 15.9 Hz, 1H), 7.55–7.48 (m, H-$C_{13,}$ H-C_{15}, 2H), 7,25 (t, H–C_4, $^3J_{4,3}$ = $^3J_{4,5}$ = 7.7 Hz, 1H), 6.90 (d, H-C_3, J = 8.2 Hz, 1H), 6,85 (t, H–C_5, $^3J_{5,4}$ = $^3J_{5,6}$ = 6.0 Hz, 1H), 6.82 (d, H–C_{10}, $^3J_{10,11}$ = 15.9 Hz, 1H,). ^{13}C NMR (101 MHz, DMSO d_6, δ (ppm)): 178.54 (C_8), 164.19 (C_9), 157.10 (C_1), 141.07 (C_7), 139.03 (C_{11}), 137.41 (C_{12}), 134.23 (C_{16}), 131.79 (C_4), 131.31 (C_{13}), 129.89 (C_{15}), 127.91 (C_{17}), 127.51 (C_6), 126.56 (C_{14}), 121.90 (C_{10}), 120.65 (C_2), 119.70 (C_5), 116,64 (C_3)

(E)-3-(3-chlorophenyl)-N'-((E)-2-((8-hydroxyquinolin-2-yl)methylene)hydrazinecarbonothioyl)acrylohydrazide (3a)

The compound was obtained as a beige powder (72% yield), mp 183.5–186 ℃. Anal $C_{20}H_{16}ClN_5O_2S$ (Mw = 425.07 g mol^{-1}): Calculated: C, 56.40; H, 3.79; N, 16.44; S, 7.53%; Found: C, 56.31; H, 3.69; N, 16.36; S, 7.45%. IR-ATR (cm^{-1}): C = S (1219.42), C = N (1633.96), C = O (1669.11), NH (3207.77), NH amide (3353.15). ^{1}H NMR (400 MHz, DMSO d_6, δ (ppm)): 12.27 (s, H-N_2, 1H), 10.60 (s, H-N_3, 1H), 10.37 (s, H-N_4, 1H), 9.86 (s, $C_{8'}$-OH, 1H), 8.55 (d, H–C_3, $^3J_{3,4}$ = 8.7 Hz, 1H), 8.35–8.30 (m, H–C_4, H–$C_{7,}$ 2H), 7.73 (s, H-C_{17}, 1H), 7.64 (d, H-C_{14} $^3J_{13,14}$ = 2.9 Hz, 1H), 7.60 (d, H-C_{11}, $^3J_{11,10}$ = 16.0 Hz, 1H), 7.51 – 7.38 (m, H-C_{13}, H-$C_{15,}$ H-$C_{5'}$, H-$C_{6'}$, 4H), 7.12 (dd, H–$C_{7'}$, $^3J_{7',6'}$ = 7.4, $^3J_{7',5'}$ = 1.1 Hz, 1H), 6.86 (d, H-C_{10}, $^3J_{10,11}$ = 16.0 Hz, 1H). ^{13}C NMR (101 MHz, DMSO d_6, δ (ppm)): 179.30 (C_8), 164.32 (C_9), 153.95 ($C_{8'}$), 152.11 (C_2), 143.89 (C_7), 139.20 (C_{11}), 138.69 (C_6), 137.38 (C_{12}), 136.62 (C_4), 134.23 (C_{16}), 131.32 (C_{15}), 129.93 (C_{13}), 129.33 ($C_{6'}$), 128.69(C_5), 127.95(C_{17}), 126.61 (C_{14}), 121.81 (C_{10}), 119.09 (C_3), 118.23 ($C_{5'}$), 112.61($C_{7'}$).

(E)-3-(3-chlorophenyl)-N'-((E)-2-(1-(pyridin-2-yl)ethylidene)hydrazinecarbonothioyl)acrylohydrazide (4a)

The compound was obtained as a beige powder (63% yield), mp 179–181.5 ℃. Anal: $C_{17}H_{16}ClN_5OS$ (Mw = 373.08 g mol^{-1}): Calculated: C, 54.62; H, 4.31; N, 18.73; S, 8.58%; Found: C, 54.52; H, 4.21; N, 18.63; S, 8.48%. IR-ATR (cm^{-1}): C = S (1205.48), C = N (1629.31), C = O (1674.29), NH (3124.03), NH amide (3382.11). ^{1}H NMR (400 MHz, DMSO d_6, δ (ppm)): 10.81 (s, H-N_2, 1H), 10.37–10.41 (br.m.ovlp., H-N_3, H-N_4, 2H), 8.61 (d, H–C_6, $^3J_{6,5}$ = 4.3 Hz, 1H), 8.55 (d, H-$C_{3,}$ $^3J_{3,4}$ = 8.1 Hz, 1H), 7.83 (t, H-$C_{4,}$ $^3J_{4,3}$ = $^3J_{4,5}$ = 7.1 Hz, 1H), 7.72 (s, H-$C_{17,}$1H), 7.64–7.61 (m, H-$C_{14,}$ 1H), 7.58 (d, H-C_{11}, $^3J_{11,10}$ = 16.0 Hz, 1H), 7.48 (d, H-C_{13} = H-C_{15}, $^3J_{13,14}$ = $^3J_{15,14}$ = 4.4vHz, 2H), 7,41 (т, H–C_5, 1H), 6.86 (d, H-C_{11}, $^3J_{11,10}$ = 16.0 Hz, 1H), 2.44 (s, H-$C_{methyl,}$ 3H). ^{13}C NMR (101 MHz, DMSO d_6, δ (ppm)): 179.68 (C_8), 164.08 (C_9), 154.96 (C_2), 150.05 (C_6), 148.95 (C_7), 139.12 (C_{11}), 137.39 (C_{12}), 136.79 (C_4), 134.23 (C_{16}), 131.32 (C_{15}), 129.91 (C_{13}), 127.92 (C_{17}), 126.58 (C_{14}), 124.59 (C_5), 121.82 (C_{10}), 121.64 (C_3), 12.72 (C_{methyl}).

(E)-3-(4-chlorophenyl)-N'-((E)-2-(pyridin-2-ylmethylene)hydrazinecarbonothioyl)acrylohydrazide (1b)

The compound was obtained as a beige powder (79% yield), mp 217–219 ℃. Anal: $C_{16}H_{14}ClN_5OS$ (Mw = 359.06 g mol^{-1}): Calculated: C, 53.41; H, 3.92; N, 19.46; S, 8.91%; Found: C, 53.34; H, 3.87; N, 19.41; S, 8.86%. IR-ATR (cm^{-1}): C = S (1282.53), C = N (1628.00), C = O (1667.33), NH (3173.63), NH amide (3368.47). ^{1}H NMR (400 MHz, DMSO d_6, δ (ppm)): 12.06 (s, H-N_2, 1H), 10.49 (s, H-N_3, 1H), 10.34 (s, H-N_4, 1H), 8.59 (d, H–C_6, $^3J_{6,5}$ = 4.8 Hz, 1H), 8.40 (d, H-C_3, $^3J_{3,4}$ = 8 Hz, 1H) 8.14 (s, H-C_7, 1H), 7.87 (t, H-C_4, $^3J_{4,3}$ = $^3J_{4,5}$ = 7.9 Hz, 1H), 7.67 (d, H-C_{13}, H-$C_{17,}$ $^3J_{13,14}$ = $^3J_{17,16}$ = 8.2 Hz, 2H), 7.59 (d, H-C_{11}, $^3J_{11,10}$ = 15.8 Hz, 1H), 7.51 (d, H-$C_{14,}$ H-C_{16}, $^3J_{14,13}$ = $^3J_{16,17}$ = 8.1 Hz, 2H,), 7,40 (t, H–C_4, $^3J_{4,3}$ = $^3J_{4,5}$ = 6.3 Hz, 1H,), 6.78 (d, H-C_{10}, $^3J_{10,11}$ = 15.8 Hz, 1H). ^{13}C NMR (101 MHz, DMSO d_6, δ (ppm)): 179.26 (C_8), 164.42 (C_9), 153.61 (C_2), 149.82 (C_6), 144.00 (C_7), 139.37 (C_{11}), 137.02 (C_4), 134.75 (C_{12}), 134.03 (C_{15}), 129.90 ($C_{13,}$ C_{17}), 129.53 (C_{14}, C_{16}), 124.74 (C_5), 120.96 (C_3), 120.89 (C_{10}).

(E)-3-(4-chlorophenyl)-N'-((E)-2-(2-hydroxybenzylidene)hydrazinecarbonothioyl)acrylohydrazide (2b)

The compound was obtained as a white powder (77% yield), mp 197–199 ℃. Anal: $C_{17}H_{15}ClN_4O_2S$ (Mw = 374.06 g mol^{-1}): Calculated: C, 54.47; H, 4.03; N, 14.95; S, 8.55%; Found: C, 54.39; H, 3.96; N, 14.85; S, 8.47%. IR-ATR (cm^{-1}): C = S (1226.23), C = N (1631.60), C = O (1669.99), NH (3178.32), NH amide (3301.54). ^{1}H NMR (400 MHz, DMSO d_6, δ (ppm)): 11.77 (s, H-N_2, 1H), 10.26 (s, H-N_3, C_1-OH, 2H), 9.94 (s, H-N_4, 1H), 8.44(s, H-C_7, 1H), 8.04 (d, H–C_6, $^3J_{6,5}$ = 5.7 Hz, 1H), 7.66 (d, H-C_{13} = H-C_{17}, $^3J_{13,14}$ = $^3J_{17,16}$ = 8.5 Hz, 2H), 7.57 (d, H-C_{11}, $^3J_{11,10}$ = 15.9 Hz, 1H), 7.51 (d, H-C_{14} = H-$C_{16,}$ $^3J_{14,13}$ = $^3J_{16,17}$ = 8.4 Hz 2H), 7,25 (t, H–C_4, $^3J_{4,3}$ = $^3J_{4,5}$ = 7.7 Hz, 1H), 6.90 (d, H–C_3, $^3J_{3,4}$ = 8.2 Hz, 1H), 6,85 (t, H–C_5, $^3J_{5,6}$ = $^3J_{5,4}$ = 7.5 Hz, 1H), 6.78 (d, H-C_{10}, $^3J_{10,11}$ = 15.9 Hz, 1H). ^{13}C NMR (101 MHz, DMSO d_6, δ (ppm)): 178.59 (C_8), 164.35 (C_9), 157.13 (C_1), 141.09 (C_7), 139.23 (C_{11}), 134.72 (C_{12}), 134.07 (C_{15}), 131.79 (C_4), 130.38 (C_{14} = C_{16}),129.87 (C_{13} = C_{17}), 129.53 (C_6), 121.00 (C_{10}), 120.54 (C_2), 119.70 (C_5), 116.70 (C_3).

(E)-3-(4-chlorophenyl)-N'-((Z)-2-((8-hydroxyquinolin-2-yl)methylene)hydrazinecarbonothioyl)acrylohydrazide (3b)

The compound was obtained as a beige powder (80% yield), mp 207–209 ℃. Anal: $C_{20}H_{16}ClN_5O_2S$ (Mw = 425.07 g mol-1): Calculated: C, 56.40; H, 3.79; N, 16.44; S, 7.53%; Found: C, 56.30; H, 3.70; N, 16.34; S, 7.42%. IR-ATR (cm^{-1}): C = S (1236.93), C = N (1633.02), C = O (1670.86), NH (3166.49), NH amide (3309.46). ^{1}H NMR (400 MHz, DMSO d_6, δ (ppm)): 12.28 (s, H-N_2, 1H), 10.62 (s, H-N_3, 1H), 10.39 (s, H-N_4, 1H), 9.89 (s, $C_{8'}$-OH, 1H), 8.56 (d, H–C_3, $^3J_{3,4}$ = 8.8 Hz, 1H), 8.37–8.30 (m, H–C_4, H–$C_{9,}$ 2H), 7.68 (d, H-C_{13} = H-$C_{17,}$ $^3J_{13,14}$ = $^3J_{17,16}$ = 8.5 Hz, 2H), 7.60 (d, H-C_{11}, $^3J_{11,10}$ = 15.9 Hz, 1H), 7.52 (d, H-C_{14} = H-$C_{16,}$ $^3J_{14,13}$ = $^3J_{16,17}$ = 8.5 Hz, 2H), 7.40 (d, H-$C_{5'}$, H-$C_{6'}$, 2H), 7.12 (d, H–$C_{7'}$, $^3J_{7',6'}$ = 7.5 Hz, 1H), 6.81 (d, H-C_{10}, $^3J_{10,11}$ = 15.9 Hz, 1H). ^{13}C NMR (101 MHz, DMSO d_6, δ (ppm)): 179.33 (C_8), 164.49 (C_9), 153.95 ($C_{8'}$), 152.11 (C_2), 143.89 (C_7), 139.42 (C_{11}), 138.68 (C_6), 136.63

(C_4), 134.76 (C_{12}), 134.01 (C_{15}), 129.93 (C_{13} = C_{17}), 129.54 (C_{14} = C_{16}), 129.34 (C_5), 128.70 ($C_{6'}$), 120.85 (C_{10}), 119.08 (C_3), 118.24($C_{5'}$), 112.63 ($C_{7'}$).

(E)-3-(4-chlorophenyl)-N'-((Z)-2-(1-(pyridin-2-yl)ethylidene) hydrazinecarbonothioyl)acrylohydrazide (4b)

The compound was obtained as a beige powder (69% yield), mp 185.5–187.5 ℃. Anal $C_{17}H_{16}ClN_5OS$ (Mw = 373.0 8 g mol^{-1}): Calculated: C, 54.62; H, 4.31; N, 18.73; S, 8.58%; Found: C, 54.52; H, 4.21; N, 18.63; S, 8.49%. IR-ATR (cm^{-1}): C = S (1233.48), C = N (1614.81), C = O (1667.26), NH (3178.47), NH amide (3303.21). ^{1}H NMR (400 MHz, DMSO d_6, δ (ppm)): 10.79 (s, H-N_2, 1H), 10.38 (s, H-N_4, H-N_5, 2H), 8.60 (s, H–C_6, 1H), 8.55 (d, H-C_3, $^3J_{3,4}$ = 7.8 Hz, 1H), 7.83 (t, H-C_4, $^3J_{4,3}$ = $^3J_{4,5}$ = 7.8 Hz, 1H), 7.67 (d, H-C_{13} = H-C_{17}, $^3J_{13,14}$ = $^3J_{17,16}$ = 7.9 Hz, 2H), 7.59 (d, H-C_{11}, $^3J_{11,10}$ = 15.8 Hz, 1H), 7.52 (d, H-C_{14} = H-C_{16}, $^3J_{14,13}$ = $^3J_{16,17}$ = 7.9 Hz, 2H),7.45–7.39 (m, H-C_5, 1H) 6.81 (d, H-C_{10}, $^3J_{10,11}$ = 15.8 Hz, 1H,), 2.45 (s, H-C_{methyl}, 3H). ^{13}C NMR (101 MHz, DMSO d_6, δ (ppm)): 179.72 (C_8), 164.23 (C_9), 154.98 (C_2), 150.03 (C_6), 148.96 (C_7), 139.31 (C_{11}), 136.78 (C_4), 134.73 (C_{12}), 134.01 (C_{15}), 129.88 (C_{13} = C_{17}), 129.53 (C_{14} = C_{16}), 124.57 (C_5), 121.63 (C_{10}), 120.93 (C_3), 12.70 (C_{methyl}).

2.5. Biological assays

2.5.1. Preparation of compounds

All compounds used in biological studies, including positive control drugs, were initially dissolved in dimethyl sulfoxide (DMSO, Sigma-Aldrich, Cat. No. D2650) to the stock concentration of 20 mM, and stored at + 4 °C. Further dilutions have been performed on the day of the experiment, using suitable medium, which is specified further in the text. The final concentration of DMSO on treated biological samples did not exceed 0.5% (v/v).

2.5.2. Cell cultures

Human colorectal adenocarcinoma (LoVo, ATCC® CCL-229^{TM}), human ovary adenocarcinoma (SkOV-3, ATCC® HTB-77^{TM}), human lung non-small cell carcinoma (A549, ATCC® CCL-185^{TM}), human mammary adenocarcinoma (MCF-7, ATCC® HTB-22^{TM}), human pancreatic adenocarcinoma (AsPC-1, ATCC® CRL-1682^{TM}) and human hepatocellular carcinoma (HepG-2, ATCC® HB-8065^{TM}) cell lines were generously gifted by Transgene SA (Illkirch, Strasbourg, France). HaCaT keratinocytes were purchased from CLS Cell Lines Service GmbH (Eppelheim, Germany, Cat. No. 300493). All cell lines were maintained in Dulbecco's Modified Eagle's Medium (DMEM) high glucose medium (Dominique Dutscher, Cat No L0102-500), supplemented with 10% (v/v) heat inactivated fetal bovine serum (FBS, Life Technologies, Cat No 10270–106) and 1% (v/v) penicillin–streptomycin (10 000 units/mL, Gibco, Cat No 15140–122). Cells were kept at 37 °C in humidified atmosphere containing 5 % (v/v) CO_2 during their exponential growing phase and in the course of incubation with investigated compounds.

2.5.3. Calcein AM (CAM) and propidium iodide (PI) staining

Cells were seeded in 96 flat bottom well plates (Corning® Costar®, Cat. No. CLS3596) in 0.1 mL volume per well (100 000 cells/mL), and left overnight to settle. On the next day, stocks of investigated compounds were diluted using complete DMEM medium to prepare working solutions which concentrations were threefold higher than the final. Those working solutions were added to cells in volume of 0.05 mL, thus the final concentrations in wells were 30, 50, 75, and 100 μM. In wells with non-treated cells, 0.05 mL of medium with 0.5 % (v/v) DMSO was added. After 24 h of incubation, staining solution was added (CAM and PI in final concentrations of 0.5×10^{-3} gr/mL and 1×10^{-6} gr/mL, respectively), and plate was left at room temperature for 30 min in dark. Results were red on Celigo® imaging cytometer (Cyntellect, Brooks Life Science Systems, Poway, CA, USA) using green and red fluorescent channels. Number of live cells has been determined by dedicated Celigo software. Cell survival was calculated using the following formula:

$$\%survival = [numberoflivecellsintreatedsample / numberoflivecellsinnontreatedsample] \times 100$$

The same experimental protocol has been implied to assess acute skin and acute liver toxicity of investigated compounds on HaCaT and HepG-2 cells.

2.5.4. Annexin v and PI staining

Cells were seeded in 96 flat bottom well plates (Corning® Costar®, Cat. No. CLS3596) in 0.1 mL volume per well (100 000 cells/mL), and left overnight to settle. On the next day, stocks of investigated compounds were diluted using complete DMEM medium to prepare working solutions which concentrations were threefold higher than the final. Those working solutions were added to cells in volume of 0.05 mL, thus the final concentrations in wells were 1, 10, 30, 50, 75, and 100 μM. In wells with non-treated cells, 0.05 mL of medium with 0.5 % (v/v) DMSO was added.

After 24 h of incubation, supernatant medium with non-adherent cells was removed from each well and placed into another 96 well plate. Ethylenediaminetetraacetic acid (EDTA, 2 mM in saline w/v) was added to wells with remaining adherent cells and plate was left at 37 ^{0}C. After 15 min, plate was centrifuged (450 g for 10 min), supernatant discarded, and 200 μL of trypsin-EDTA (BioWest, Nuaille, Cat No L0930-100) added to each well. Cells were detached in about 15 min of incubation at 37 °C. Trypsin-EDTA was discarded after additional spinning cycle, when previously removed supernatants with non-adherent cells were turned back to trypsinized cells. Such prepared samples were stained with Annexin V-FITC (Immuno Tools, Cat No 31490013) and PI (Miltenyl Biotec IncCat No 130–093-233) each in a volume of 3 μL. Here described trypsinization protocol was applied every time cells were prepared for flow cytometry analyses, unless is stated otherwise.

Plates were analyzed on Guava® easyCyte 12HT Benchtop flow microcapillary cytometer (Millipore, Merck, Darmstadt, Germany) using the dedicated InCyte® software package. Cells were classified according to Annexin V-FITC (green fluorescence) and PI (red fluorescence) labeling on viable (double negative), pre-apoptotic cells (Annexin V-FITC single-stained cells), necrotic cells (PI single-stained cells), and cells in advanced phases of cell death (double-stained cells).

2.5.5. Concentration-response curve plotting

Results from Annexin V/PI readouts were used to generate concentration–response curves. Percentages of all cells stained

with either Annexin V and/or PI were summarized for each treated sample and plotted against corresponding concentration. Curves were defined in GraphPad Prism 8 software (GraphPad Software, San Diego, CA, USA) using a sigmoidal asymmetric five-parameter logistic equation, or by biphasic sigmoid least squares fit equation, as is specified further in the text. Cell death concentration (CdC_{50}) is the one that induces death in 50% of treated cells.

2.5.6. Assessment of cells in sub-G1 area

After Annexin V/PI reading was over, plates with remaining cells were centrifuged (450 × g for 10 min), the supernatant discarded, and 200 µL of 70% ethanol was added to cells. The plates were left overnight at 4 °C. On the next day, the plates were centrifuged on 450 × g for 10 min, ethanol was discarded, and ribonuclease A (RNase A, Sigma-Aldrich, Cat. No. R4875) in PBS was added to wells (0.5×10^{-6} g/mL, final concentration). After plates were incubated at 37 °C for 1 h, cells were stained with PI (1×10^{-6} g/mL final concentration) and kept in the dark at room temperature for 30 min before analysis. Cells were acquired on Guava® easyCyte 12HT Benchtop flow microcapillary cytometer, and the population was analyzed with the dedicated InCyte® software package.

2.5.7. Cell cycle analysis

The distribution of cells within mitotic division phases has been evaluated after 12 h of treatment with investigated compounds added in a range of six concentrations. At the end of incubation time, 96 well plates with investigated samples were centrifuged (450 × g for 10 min), and the media was discarded. Cells were detached by trypsin treatment and fixed with 70 % ethanol overnight, followed with RNase A treatment and PI staining as described above. Cells were acquired on Guava® easyCyte 12HT Benchtop flow microcapillary cytometer, and populations analyzed with the dedicated InCyte® software package.

2.5.8. Determination of cellular activated caspase-8 or/and caspase-9

Investigated compounds were added to wells with attached cells in concentration of 50 µM. After 6 h of treatment, cells were detached by trypsin treatment, and stained with caspase-8 (CaspGLOW^{TM} fluorescein active caspase-8 staining kit, BioVision, Cat. no. K188-25) and caspase-9 (CaspGLOW^{TM} red active caspase-9 staining kit, BioVision, Cat. no. K199-25), according to the manufacturer's instructions. Cells were analyzed on Guava® easyCyte 12HT Benchtop flow microcapillary cytometer using the dedicated InCyte® software package. The statistical evaluation has been performed using an unpaired *t*-test with Welch's correction comparing treated to the non-treated population of cells.

2.5.9. Assessment of mitochondrial superoxide radical ($^{\bullet}O_2^-$) generation

Investigated compounds were added to wells with attached cells in concentration of 50 µM. After 6 h of treatment, cells were detached by trypsin treatment, and stained with MitoSox Red (ThermoFisher Scientific, Cat. No. M36008), according to the manufacturer's recommendations. Analysis was performed on Guava® easyCyte 12HT Benchtop flow microcapillary cytometer. Pro-oxidant activity is analyzed over the percentage of cells positive for $^{\bullet}O_2^-$ and over the mean fluorescent intensity (MFI) expressed in arbitrary units (AU). MFI parameter is computed for $^{\bullet}O_2^-$-positive subpopulation and corresponds to average flow of $^{\bullet}O_2^-$ per cell. Statistical comparison of MFI values was performed using the Kruskal-Wallis test with an unpaired *t*-test with Welch's correction as a post-test.

2.5.10. Assessment of anti-migratory activity

Cells were seeded in 96 flat bottom well plates (Corning® Costar®, Cat. No. CLS3596) in 0.1 mL volume (100 000 cells/mL) using complete DMEM medium. Cells were kept for additional few days to form confluent layer with medium exchanged daily. When confluency has been reached, complete medium was exchanged with FBS-free DMEM and left on cells for 18 h. Thereafter, a scratch in a cell layer was made using 0.2 mL pipette tips, cells were gently washed twice with serum-free medium, stained with CAM and imaged on Celigo® cytometer. Then, medium was discarded and replaced with solution of investigated compounds (1 and 10 µM, final concentrations) prepared in DMEM supplemented with 1% FBS. After 24 h incubation, cells were stained with CAM and images were taken on Celigo®. Changes in size of scratched area between 0 and 24 h of treatment were analyzed using TScratch software. Results are expressed as % of open wound area at 24 h, while statistical significance was determined by means of Kruskal-Wallis test and unpaired *t*-test with Welch's correction.

2.5.11. Mtb strain selection

Anti-*Mtb* activity was evaluated against three *Mtb* clinical isolates selected from the culture collection owned by the Institute of Microbiology and Immunology, Faculty of Medicine Belgrade. The initial selection included 25 randomly chosen *Mtb* isolates, whose identification was verified by the GenoType MTBC assay (Hain Lifescience, Nehren, Germany). Susceptibility to INH and RIF was evaluated by the proportion method on Löwenstein-Jensen (LJ) medium, and by using the GenoType MTBDRplus (Hain Lifescience) for detection of mutations conferring resistance to the drugs (Almeida Da Silva and Palomino, 2011; Seifert et al., 2015). The selected panel of three *Mtb* strains included a drug sensitive strain designated as *Mtb-InhRif-S*, a strain resistant to INH and susceptible to RIF designated as *Mtb-Inh-R*, and a strain susceptible to INH and resistant to RIF designated as *Mtb-Rif-R*.

The isolates were stored in glycerol stocks at −70 °C, and re-cultured on LJ medium for four-six weeks at 37 °C prior to further testing.

2.5.12. Assessment of anti-Mtb activity

Colonies of *Mtb* strains were peeled off in a thin layer from LJ medium and transferred into Middlebrook 7H9 broth (Liofilchem, Cat. No. 620214) supplemented with 10 % (v/v) ADC Enrichment (Difco, Cat. No. 212352), 0.2 % glycerol (Sigma-Aldrich, Cat. No. G5516), and 0.05 % (v/v) Tween 80 (Sigma-Aldrich, Cat. No. P6474). Large bacterial clumps were broken by passage through a 27 Gauge needle, after which single cell suspensions were established using a 5 µm sterile filter (Millex-SV 5.0 µm, Millipore, Cat. No. SLSV025LS). Suspensions were incubated at 37 °C in humidified atmosphere containing 5 % (v/v) CO_2) over one week. On

the day of the experiment, the densities of the strains were adjusted to 0.1 McFarland standard and further diluted 1:25, as recommended previously (Trotsko et al., 2020). Each microtiter plate (Thermo Scientific, Cat. No. 130188) was organized as the following: 0.25 mL of sterile water was added in outer perimeter wells (rows A and H, columns 1 and 12), to minimize evaporation of the medium in tested wells; 0.12 mL of supplemented 7H9 medium was added per well to 6 wells (blank); 0.1 mL of bacilli suspension, at arranged density as described above, was seeded per well in the rest of the plate. Investigated compounds, INH (Supelco, Cat. No. I3377) and RIF (Sigma-Aldrich, Cat. No. 557303), all previously dissolved in DMSO at 20 mM, were diluted to working concentrations using the same supplemented 7H9 broth medium immediately prior addition to microtiter plates. In 6 out of 54 wells with seeded bacilli, 0.02 mL of supplemented 7H9 medium was poured per well (non-treated control), while in the rest of 48 wells drugs were added in 0.02 mL volume thus their final concentrations in wells were 0.03–100 μM. The highest concentration of DMSO in the samples subjected to concentrations of 100 μM was 0.5 % (v/v).

After 6 days of incubation, 3-(4,5-dimethylthiazol-2-yl)-2,5-diphenyltetrazolium bromide (MTT, Sigma, Cat. No. M2128) was added to blank, treated and non-treated wells (0.05 mL, 5 mg/mL in Phosphate buffered saline). Following 24 h of incubation, 0.01 mL of 10 % (w/v) sodium dodecyl sulfate (SDS, Sigma-Aldrich, Cat. No. 436143) in water was used to dissolve formazan crystals over additional 24 h at 37 °C. The optical densities were measured at 570 nm (ThermoFisher Multiscan™ Microplate Reader). The experiment was performed two times. Percentage of viable bacilli for each of two replicates was computed according to the following equation (Danchuk et al., 2019):

$$\%survival = [ODtreatedsamples - ODblank/ODnon - treatedsamples - ODblank] \times 100$$

The percentage of *Mbt* growth inhibition was calculated as:

$$\%dead = 100 - \%viability$$

Computed % viability data were plotted against corresponding concentrations, and dose–response curves were drawn using the sigmoidal asymmetric five-parameter logistic equation. A 10 % bacilli survival was computed as the unknown from the sigmoidal curve (Prism 8, GraphPad Software, San Diego, USA).

For those compounds that reduced viability for 90 %, experimental procedure was repeated in the range of 10 concentrations with 2 μM of concentration interval (4 concentrations above and 5 below the one estimated by the software). Minimal inhibitory concentration (MIC) was defined as the lowest one that reduced viability of treated bacilli by 90 % or more computed by the equation described above. Values were determined using the average of three replicate wells at each concentration of the tested drug.

2.6. Molecular modelling

To assess pharmacokinetics and drug-likeness of compounds, absorption, distribution, metabolism and excretion (ADME) properties were predicted using SwissADME web-server (http://www.swissadme.ch/) (Daina et al., 2017) and pkCSM (http://biosig.unimelb.edu.au/pkcsm/) (Pires et al., 2015). We used PharmMapper online database (http://www.lilab-ecust.cn/pharmmapper/) to identify potential molecular targets. All protein targets from v2010 database (7302 targets) were matched against the pharmacophore models for 300 conformers of compounds **2a** and **3b**. The potential targets were filtered based on following criteria: normalized Fitscore > 0.7 and *z*' score > 1.

2.7. Spectrophotometric determination of stability constants of compounds complexes with Fe^{2+} and Fe^{3+} ion

At the beginning stock solutions were prepared. First, 1.0×10^{-2} M solutions of iron salts ($FeSO_4x7H_2O$ and $Fe(NO_3)_3x9H_2O$) in deionized water, and then the 2.0×10^{-4} M solutions of synthesized compounds in DMSO. Working solutions of compounds were prepared by appropriate dilution of stock solutions with DMSO to the λ_{max} absorbance value in the range 0.5–0.6. The UV spectra were recorded, and the appropriate initial concentration of compounds was calculated.

The procedure for mole-ratio method described by Momidi et al. with minor modifications was followed (Momidi et al., 2017). Briefly, into a 3 mL of compound working solution an aliquot of 2 μL of stock metal solution was added. The reaction mixture was then stirred on the magnetic stirrer at 200 rpm for 10 min and the UV spectra were recorded. The previous step was repeated until equilibrium was reached and no significant changes in the spectrum were detected.

3. Results and discussion

3.1. Chemistry, design

The compounds **1-4b** were designed as a molecular hybrids of a potent natural product – cinnamic acid, and MTCHs as synthetic small organic molecules with plethora of biological activities. Cinnamic acid and its chloro derivatives were condensed with four MTCHs to get twelve novel cinnamic acid hydrazides (**1–4b,** Fig. 2). It is known that MTCHs exhibit keto/enol tautomerism, and they could adopt *E*- or *Z*- configuration around the C = N bond (Abu El-Reash et al., 2014). *E*/*Z* isomerism is also possible for cinnamoyl moiety, but previous studies showed that cinnamic acid derivatives are over 99% in *E*- form as this is energetically more favorable isomer (Li et al., 2015; Matsuhira et al., 2008). NMR spectra also confirmed that all compounds exist solely as *E*-isomers around *α, β*-unsaturated moiety in the cinnamic acid part of the molecule. This is evidenced by the appearance of olefinic proton doublets at ~ 6.80 ppm and ~ 7.60 ppm with the $^3J_{HH}$ coupling constant of 15.9 Hz.

The solution structure of compounds **1-4b** is elucidated with the aid of 2D NMR spectroscopy techniques (COSY, NOESY, ^1H–^{13}C HSQC, and ^1H–^{13}C HMBC). ^1H and ^{13}C NMR spectra for all compounds and representative 2D NMR spectra for compounds **1, 2a, 3** and **4** are given in ESI (Fig. S1-S35). According to NOESY spectra given in Figure S35, all compounds exist in *E*-form around azomethine bond. This is suggested by cross-peaks between N_2-H with proton or protons of methyl group attached to carbon C_7.

The same trend is observed for 3-chloro and 4-chloro cinnamic acid derivatives. Therefore, it can be concluded that all compounds are in the form of stable (*E*,*E*)-isomers.

3.2. ADME properties

The pharmacokinetics and drug-likeness data predicted for compounds **1-4b** are shown in Table 1. Compounds with poor aqueous solubility, low permeability and high lipophilicity have low bioavailability and usually are filtered-off in early stages of drug development projects. According to Biopharmaceutics Classification System (BCS), compound is considered as highly permeable when the percentage of absorption is over 90%. According to Table 1, 9 out of 12 derivatives can be considered as highly permeable compounds with appropriate absorption through human intestinal membrane.

Lipinski rule of 5 (RO5) predicts the oral bioavailability of a drug molecule (Lipinski et al., 2001). All compounds obey RO5 and are likely to be well absorbed upon oral administration. Moreover, estimated solubility (ESOL) predictions classified all compounds as moderately soluble, and have poor blood–brain barrier (BBB) permeability which suggests low toxicity on central nervous system.

3.3. Investigation of anti-Mtb activity

Capacity of the compounds tested to deplete outstanding survival abilities of *Mtb* has been estimated against the panel of three clinical *Mtb* isolates. The isolates were selected as suitable for investigation of new drugs' activity, according to their phenotypic sensitivity or resistance to INH and RIF in conjunction with specific mutation patterns. The resistance genotypes of the three strains were as follows (Figure S36): (1) *Mtb-InhRif-S* harbored no mutations associated with resistance to INH and R; (2) *Mtb-Inh-R* harbored *kat*G mutation S315T mediating resistance to INH; (3) *Mtb-Rif-R* harbored *rpo*B mutation S531L conferring resistance to RIF.

MTT results for the *Mtb-Inh-R* (Figure S37, Table 2) showed that MIC value for RIF corresponds to that reported in wild type $H_{37}Rv$ reference strain, while MIC for INH was 4–6 fold higher than in $H_{37}Rv$ (Castelo-Branco et al., 2018; De et al., 2011), which is consistent with the *kat*G mutation detected. However, results of the MTT assay for the *Mtb-Rif-R* and *Mtb-InhRif-S* strains revealed discrepancies between the actual phenotypic response to treatments and the response anticipated according to the genetic typing. The maximal achieved reduction of *Mtb-Rif-R* growth at 100 μM was 43.63 ± 2.53 % for RIF and 82.39 ± 0.62 % for INH, compared to non-treated control (Figure S38). Although the *Mtb-Rif-R* showed better response to INH than to RIF, the overall outcome demonstrates a highly resistant phenotype of the strain, discordant the genotyping results. The phenotypic-genotypic discrepancy for response to INH treatment was even more profound in *Mtb-InhRif-S*. Namely, the maximal growth inhibition accomplished by INH was as low as 14.87 ± 3.62 % at 100 μM (Figure S39). The genotypic–phenotypic inconsistencies in INH or RIF susceptibility we noted, have already been described in *Mtb* strains, with various explanations suggested (Hofmann-Thiel et al., 2017; Jo et al., 2017; Kang et al., 2019). Considering the results of GenoType MTBDRplus test, the most plausible explanation is the presence of mutations at other regions in *rpoB*, *katG* or *inh*A genes, not covered by the assay.

Results acquired after *Mtb* treatment with four primary structural moieties (**1**–**4**) reveal significant differences in their abilities to induce death in the treated strains (Figures S37-S39). The activities of compounds **1** and **2** were negligible in all the strains, with exception of reduced survival for 86.67 ± 3.12 % exhibited by **1** at 100 μM on *Mtb-Inh-R*. The dose–response curves that describe activity of **4** in *Mtb-Inh-R* and *Mtb-Rif-R* strains are similar in that they have two plateau phases. It is noteworthy that second plateau in *Mtb-Inh-R* was defined between 30 and 100 μM with the MIC value achieved (Table 2), while in the strain *Mtb-Rif-R* the plateau was positioned between 10 and 100 μM without reaching the MIC value. Although compound **4** did not reach MIC value in *Mtb-InhRif-S*, it eliminated high proportion of the bacilli treated at 100 μM. According to the MIC values established, the only compound employed in the current study which showed ability to deplete survival for > 90 % in all three *Mtb* strains was compound **3**. In contrast to INH and RIF, compound **3** attained MIC in *Mtb-Rif-R* strain. While in *Mtb-Inh-R* strain, **3** appears less efficient compared to INH and RIF (Table 2), it should be noted that its dose–response curve is overlapping with those of the two positive control treatments within a range 30–100 μM (Figure S37). The MIC for **3** in *Mtb-InhRif-S* strain is higher than that established for RIF, whereas the dose–response curves show that the compound **3** was more efficient than RIF at concentrations 1 and 10 μM (Figure S39).

In respect of structure–activity relationship, compound **2** that is carrying 2-hydroxyphenyl group had the least impact on survival of treated *Mtb* strains. Replacement of 2-hydroxyphenyl with 2-pyridyl ring, as is in compound **1**, did not lead to noteworthy improvement of anti- *Mtb* abilities. However, addition of methyl group at C7 position in **1** yielded to compound **4** and notable augmentation of activity. Finally, compound **3**, which has 8-hydroxy-2-quinolyl instead of 2-hydroxyphenyl or 2-pyridyl rings, was the only one with capacity to deplete *Mtb* survival in all three treated strains. Additional introduction of chlorine in *meta*- or *para*- position of phenyl ring to core **1**–**4** structures had different influence on activities of gained derivatives compared to activity of corresponding parental compound. While this structural manipulation with compound **2** did not make notable improvements, the same led to drastic loss in anti-*Mtb* activities of **3a** and **3b** (Figures S37-S39). On the other hand, **1b** and **4a** revealed greater activity in *Mtb-Rif-R* than **1** and **4**, respectively (Figure S38), and achieved MICs in *Mtb-Inh-R* strain (Table 2).

3.3.1. Plausible mechanism of anti-Mtb action

Cell wall of *Mtb* bacillus is of very unique structure and composition. It contains peptidoglycan layer that is essential for maintaining cellular integrity, virulence, and resistance to drugs which are highly efficient against other microbial pathogens (Maitra et al., 2019). A number of ligands that are rationally created, and later on been proven as potent inhibitors of targeted *Mtb* enzyme in *in vitro* conditions, were unable to affect bacillus survival due to high polarity and inability to permeate *Mtb* cell wall (Dalberto et al., 2020). As it can be seen in Table 1, all of our compounds have higher partition coefficient than INH, while no evident correlation can be found

Table 1 Pharmacokinetics data and drug-likeness descriptors calculated for compounds **1-4b**, isoniazid, and rifampicin.

	1	**2**	**3**	**4**	**1a**	**2a**	**3a**	**4a**	**1b**	**2b**	**3b**	**4b**	**INH**	**RIF**
AlogP	2.47	3.01	3.53	2.71	3.17	3.65	4.11	3.30	3.16	3.63	4.11	3.29	−0.71	3.29
[a] Virtual logP	1.95	2.22	2.86	1.86	2.55	2.91	3.50	2.64	2.56	3.01	3.54	2.91	−0.37	1.92
[b] **TPSA,** Å^2	102.1	112.9	119.3	101.9	102.6	113.8	122.0	102.4	101.6	112.8	122.5	101.3	71.3	220.15
ESOL solubility (μmol/L)	540	260	47	320	140	67	12	80	140	67	12	80	39,000	0.0067
Caco2 permeability (log P_{app} in 10^{-6} cm/s)	0.768	0.892	1.311	0.89	0.904	0.904	1.194	0.902	0.987	0.988	1.204	0.986	1.227	0.383
Intestinal absorption (human) %	94.362	91.822	73.208	94.032	93.38	90.841	74.416	93.051	92.98	90.441	74.39	92.651	78.2	56.061
Fraction unbound (Fu)	0.226	0.214	0.09	0.212	0.196	0.187	0.078	0.181	0.203	0.184	0.084	0.186	0.641	0.12
BBB permeability (log BB)	−1.106	−0.101	−1.224	−1.122	−1.265	−1.169	−1.384	−1.282	−1.29	−1.193	−1.408	−1.306	−0.3	−2.087
CNS permeability (log PS)	−2.599	−2.438	−2.429	−2.51	−2.492	−2.331	−2.322	−2.403	−2.486	−2.325	−2.316	−2.397	−2.925	−3.41
Bioavailability Score	0.55	0.55	0.55	0.55	0.55	0.55	0.55	0.55	0.55	0.55	0.55	0.55	0.55	0.17
# of Lipinski violations	0	0	0	0	0	0	0	0	0	0	0	0	0	3 violations: MW > 500, NorO > 10, NHorOH > 5

ESOL – Estimated solubility, TPSA – Total Polar Surface Area, P_{app} - Apparent permeability coefficient, BBB – Blood brain barrier, CNS – Central nervous system
[a] Calculated in Vega ZZ 3.2.0 using molecular lipophilicity potential (MLP)
[b] Calculated in Vega ZZ 3.2.0

Table 2 Minimal inhibitory concentrations (MIC) for isoniazid (INH), rifampicin (RIF), and investigated compounds after 6 days treatment of specified strains.

Treatment	*Mtb-Rif-R*	*Mtb-Inh-R*	*Mtb-InhRif-S*
	[μM]	[μM]	[μM]
INH	n.d.*	4	n.d.
RIF	n.d.	2	26
3	30	10	92
4	n.d.	42	n.d.
4a	n.d.	90	n.d.
1b	n.d.	88	n.d.

* n.d. - not determined in the range of tested concentrations.

comparing lipophilicity of **3**, **4**, **1b**, and **4a** to those with low activity (Table 2 and Figures S37-S39). It can be concluded that penetration through the *Mtb* cell wall is not the reason for diverse impact of here investigated compounds on survival of treated strains.

As iron uptake is essential for the survival of *Mtb,* the parasite synthesizes mycobactin syderophores to facilitate iron transport inside the cell. It was previously shown that intracellular iron chelators prevent mycobacterial growth (Dragset et al., 2015). Structurally similar aroylhydrazones are proven as excellent iron chelators (Hruskova et al., 2016), while even better iron-chelating ability may be expected for compounds **1-4b** due to presence of thione group and two additional N atoms. For that reason, we went further and performed additional studies. We have tested chelating capacity of synthesized compounds towards Fe^{2+} and Fe^{3+} ions, and the values of corresponding stability constants are given in Table 3. An example of UV–Vis spectra and the corresponding molar ratio plot for the most potent compound **3** and Fe^{2+} are given in the Fig S40. The K_s values vary slightly from $10^7 - 10^9$, and it is obvious that all compounds have strong chelating capacity and form stable complexes. Therefore, chelating ability cannot be the explanation for high activity of only one compound, and it can be concluded that an iron uptake is not the mechanism of anti-*Mtb* action.

It can be concluded that the interactions of compounds **1-4b** with particular molecular target are responsible for the observed anti-*Mtb* action. Additional experimental and *in silico* studies are required to gain deeper insights into the underlying mechanism of activity.

3.3.2. Hepatotoxicity

One of the most common side effects of anti-TB treatment by INH is hepatotoxicity (Wang et al., 2016). The mechanism responsible for liver injury relies in products of INH metabolic transformation in hepatocytes through two major pathways. Both of these pathways are enzyme-dependent reactions and include acetylation and hydrolysis of INH by *N*-acetyltransferase 2 and acyl amidase, respectively. The HepG-2 cell line is previously confirmed as reliable for evaluation of hepatotoxicity (Van Summeren et al., 2010), and Castelo-Branco et al (Castelo-Branco et al., 2018) published hepatotoxic potential of INH on this *in vitro* model. Therefore, we treated HepG-2 cells for 24 h to initially assess whether it can be expected for our compounds to induce liver damage as a serious side effect. According to the results of CAM/PI

Table 3 Stability constants of synthesized compounds complexes formed with Fe^{2+} and Fe^{3+} ions.

Compound	K_s (Fe^{2+})	K_s (Fe^{3+})
1	$1.1 \cdot 10^9$	$3.0 \cdot 10^8$
2	$4.3 \cdot 10^8$	$1.7 \cdot 10^7$
3	$4.9 \cdot 10^9$	$5.5 \cdot 10^8$
4	$6.9 \cdot 10^9$	$1.9 \cdot 10^9$
1a	$1.3 \cdot 10^9$	$4.8\ 10^9$
2a	$4.0 \cdot 10^8$	$1.2 \cdot 10^9$
3a	$4.9 \cdot 10^8$	$3.5\ 10^9$
4a	$1.7 \cdot 10^9$	$5.4 \cdot 10^9$
1b	$3.4 \cdot 10^9$	$3.8 \cdot 10^9$
2b	$1.5 \cdot 10^9$	$1.2 \cdot 10^9$
3b	$1.8 \cdot 10^9$	$5.1 \cdot 10^9$
4b	$2.8 \cdot 10^9$	$2.5 \cdot 10^9$

dual staining, none of the molecules that achieve MIC in one or all *Mtb* strains (Table 2) does concurrently reveal the ability to induce death in HepG-2 cells within a range of tested concentrations from 30 to 100 μM (Figures S41-S44).

3.4. Investigation of anticancer activity

The ability of our compounds to induce death of malignant cells was initially tested on a panel of human cell lines of different phenotypes. Evaluation was performed by means of CAM/PI dual staining method (En et al., 2017) after 24 h incubation of compounds with malignant cells.

Results gained for **1**–**4** (Table S1) show that 2-hydroxyphenyl derivative **2** stimulates response in three out of five malignant models, 8-hydroxy-2-quinolyl derivative **3** induces death in two cell lines, while 2-pyridyl derivative **1** achieves effect only in one cell type. The highest sensitivity to treatment with **1**, **2**, and **3** is found in lung adenocarcinoma cells, where all three compounds reduce viable population for > 50 % at concentration of 100 μM. Introduction of methyl group in position C7 of 2-pyridil derivative (compound **4**) significantly reduces anticancer activity in all studied cell lines compared to compound **1**.

Addition of chlorine substituent at *meta*- or *para*-position of cinnamoyl ring resulted in several analogs with significantly altered anticancer activity. The best examples in the activity shifts were observed in analogues of **2** and **3** (Table S1). While activity of *para*-chloro derivative (compound **2b**) is not considerably changed compared to **2**, *meta*-chloro derivative **2a** is the most potent anticancer agent in this series. Opposite trend is observed for compound **3**, where *meta*-substitution diminishes anticancer capacity while *para*-derivative **3b** devastates population in four out of five treated cell lines.

Regarding sensitivity of cell lines, none of investigated compounds impair vitality of pancreatic adenocarcinoma AsPC-1 cells, whereas only **2a** and **3b** reduce viable population of breast adenocarcinoma MCF-7 cells (Table S1). Ovarian adenocarcinoma SkOV-3 cells reveal low sensitivity to treatment with **2**, **3**, and **2b**, while **2a** and **3b** cause notable incidence of cell death only at 100 μM. Aside **2**, **3a** and **2b**, compound **3b** is the only that produces substantial effect on survival of colorectal adenocarcinoma LoVo cells. Finally, lung adenocarcinoma A549 cells display the greatest susceptibility to synthesized cinnamic acid hydrazides, though only **2a** and **3b** cut down their survival for > 50 % in concentrations below 100 μM.

The advantages of CAM/PI staining method, as well as other cytotoxicity assays, are affordability and fast screening of numerous samples, whereas CAM/PI in addition provides visual information on whether the tested compound inhibits cell proliferation or induces cell death. However, none of cytotoxicity tests can provide truly reliable evidence of cell death incidence for two major reasons: 1) outcome is always computed in respect to exponentially growing non-treated control, where doubling time of treated cell line can interferes the outcome; 2) those assays cannot recognize cells in early apoptosis. For those reasons, we deliberately did not compute IC_{50} concentrations, but data presented in Table S1 should be considered as informational value that served to estimate which cell phenotype shows the highest sensitivity towards tested compounds, and which compounds should be evaluated for anticancer activity. Based on these results, our investigation was continued on compounds **2a** and **3b** in A549 cells.

In order to determine the exact frequency of cell death, as well as whether **2a** and **3b** stimulate apoptosis or necrosis in A549 cells, Annexin V/PI dual staining was carried out after 24 h incubation. As it can be seen in Fig. 3A, percentages of Annexin V-single and -double stained events are increasing following the rise of applied concentrations of either **2a** or **3b**. These results clearly show that early necrosis was not the dominant type of death in A549 cells subjected to either **2a** or **3b**. The same samples analyzed on Annexin V/PI labeling were a day later examined to see was DNA fragmentation in progress or not. Cleavage of chromosomal DNA into nucleosomal and oligonucleosomal size fragments is a hallmark of advanced apoptotic death and can be seen as Sub-G0/G1 accumulation, serving as an indicator whether double-stained cells in Annexin V/PI dot-plots represent advanced apoptosis or advanced necrosis (Murad et al., 2016; Zhang and Xu, 2000). Acquired results demonstrated that percentages of events at the Sub-G0/G1 (Fig. 3B) were in strong correlation with percentages of double stained cells (Fig. 3A), which serves as conformation that both **2a** and **3b** trigger apoptotic death in A549 cells.

The activity of **2a** is described by nicely contoured sigmoidal curve whose exponential phase is plotted within concentration range from 10 to 100 μM (Fig. 3C). Impact of **3b** on death of A549 cells defines a straight line when five-parameter sigmoidal equation is used (Fig. 3C), but biphasic model perfectly fits experimental results of this compound (Fig. 3D). Such form of concentration–response curve implies that **3b** may has a concentration-dependent shift in the mechanism of its pro-apoptotic activity.

Changes in distribution of cells throughout the phases of mitotic division in regard to non-treated samples can serve as an initial indicator which cellular process has been interfered by the investigated compound. Although accumulation of cells at any particular phase of cell cycle cannot precisely addresses targeted intracellular transduction pathway, it was expected that this result may provide information about possible alteration in mechanism of pro-apoptotic activity of **3b**, altogether with potential differences in a way that **3b** and **2a** induced apoptotic response. However, there is no particular diversity comparing cell cycle distribution of cells subjected to either of two compounds (Fig. 4A). Both **2a** and **3b** promote slight accumulation of cells at the S phase already at 1 μM, and

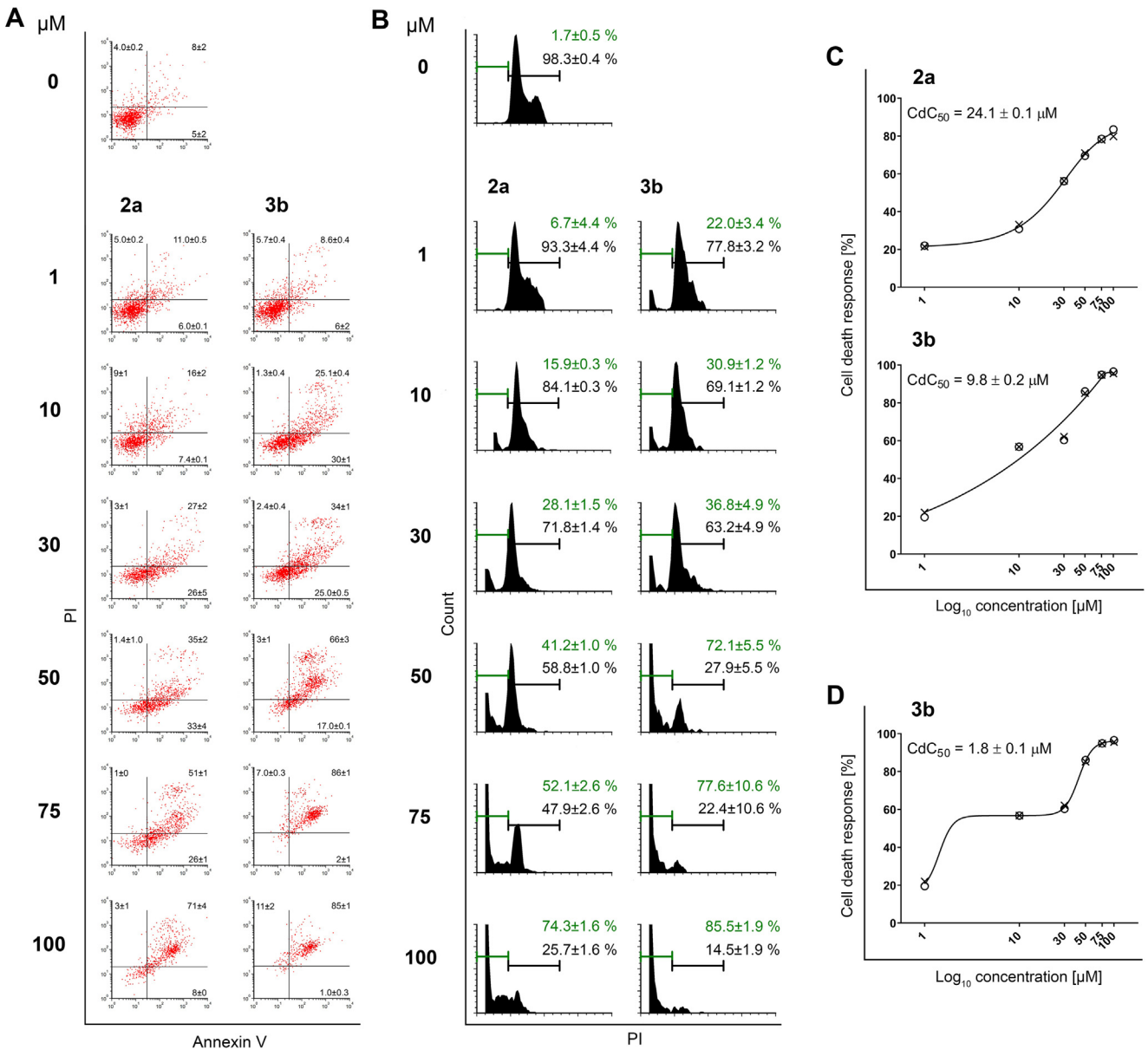

Fig. 3 Anticancer activity of compounds **2a** and **3b** in A549 cells after 24 h of treatment. (A) Representative figures of Annexin V/propidium iodide (PI) dual staining. Numbers show the mean ± SD percentages of two replicates from independent experiments. (B) Representative images and percentages of events at the Sub-G0/G1 population (green), and percentages of live cells distributed in phases of mitotic division (black). Each data point represents the mean ± SD of two replicates from independent experiments. (C) Concentration-response curves plotted by the asymmetric five-parameter sigmoidal equation in GraphPad Prism 8 software, according to data acquired by means of Annexin V/PI staining from two independent experiments (circles and crosses). (D) Concentration-response curve plotted by the biphasic sigmoidal least squares fit equation in GraphPad Prism 8 software, according to data acquired by means of Annexin V/PI staining from two independent experiments (circles and crosses). CdC50 values (C and D) express the mean ± SD concentration that induces cell death in 50% of treated cells. Instead of Log10 values on X axes (C and D), the exact concentrations are specified to assure compliance with concentrations indicated in corresponding text.

such distribution remains in samples treated with **2a** at 10 μM. At 30 μM, **2a** halts the cells at the G1-to-S check point, which proceeds toward arrest at the G1 phase started from 50 μM. Compound **3b** also induced accumulation at the G1-to-S transition but at 10 μM, while arrest at the G1 phase is assembled at 30 μM. Described changes signify that both compounds at lower concentrations caused obstacles during DNA replication process, prolonged its duration and led to accumulation of cells at the S phase. Starting from 10 μM for **3b** and 30 μM for **2a**, cells were prevented to proceed with mitotic division and those concentrations correlate with CdC_{50} values computed by means of five-parameter sigmoidal equation (Fig. 3C).

At this point of investigation, it seemed that mechanism that underlies pro-apoptotic activity of **2a** and **3b** may be quite similar or even the same, while the latter compound tends to be

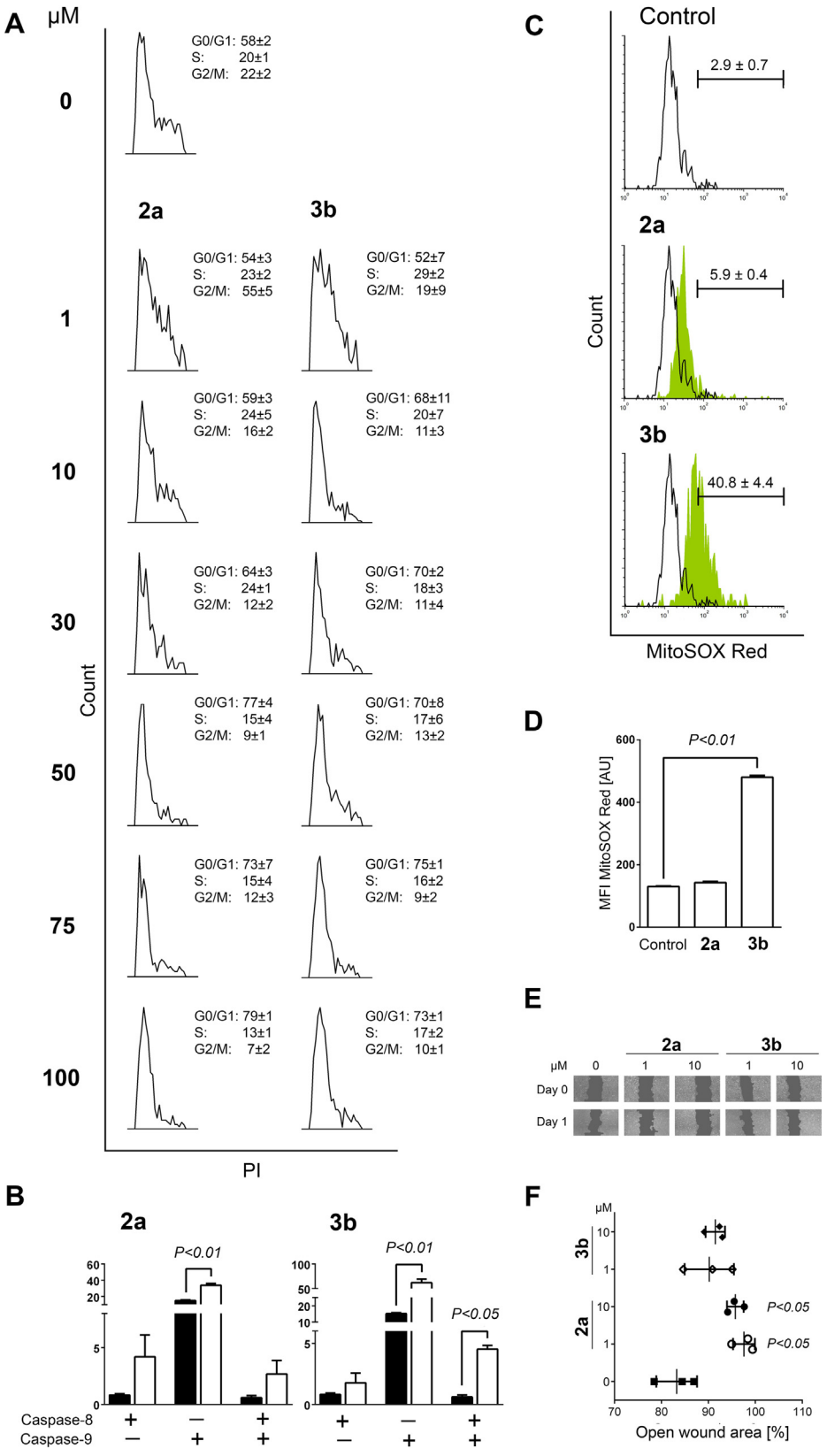
A
μM
0
1
10
30
50
75
100
2a
3b
G0/G1: 58±2
S: 20±1
G2/M: 22±2
G0/G1: 54±3
S: 23±2
G2/M: 55±5
G0/G1: 52±7
S: 29±2
G2/M: 19±9
G0/G1: 59±3
S: 24±5
G2/M: 16±2
G0/G1: 68±11
S: 20±7
G2/M: 11±3
G0/G1: 64±3
S: 24±1
G2/M: 12±2
G0/G1: 70±2
S: 18±3
G2/M: 11±4
G0/G1: 77±4
S: 15±4
G2/M: 9±1
G0/G1: 70±8
S: 17±6
G2/M: 13±2
G0/G1: 73±7
S: 15±4
G2/M: 12±3
G0/G1: 75±1
S: 16±2
G2/M: 9±2
G0/G1: 79±1
S: 13±1
G2/M: 7±2
G0/G1: 73±1
S: 17±2
G2/M: 10±1
Count
PI
B
2a
3b
P<0.01
P<0.01
P<0.05
Caspase-8
Caspase-9
C
Control
2.9 ± 0.7
2a
5.9 ± 0.4
3b
40.8 ± 4.4
Count
MitoSOX Red
D
P<0.01
MFI MitoSOX Red [AU]
Control
2a
3b
E
2a
3b
μM
Day 0
Day 1
F
μM
3b
2a
P<0.05
P<0.05
Open wound area [%]

more efficient than former. Additional confirmation of this assumption was found in results of caspase-8/-9 activation that was acquired after A549 cells were treated for 6 h with **2a** or **3b** at 50 μM. As it is presented in Fig. 4B, both compounds arouse strong activation of intrinsic apoptotic pathway, whereas significant cross-talk recruitment of caspase-8 is evident only in cells subjected to compound **3b**. However, assessment of $^{\bullet}O_2^-$ reveals substantial difference between activities of **2a** and **3b**. While **2a** has trivial impact on generation of $^{\bullet}O_2^-$, **3b** induces meaningful increase of $^{\bullet}O_2^-$-producing subpopulation of A549 cells (Fig. 4C). Additionally, MFI computed for $^{\bullet}O_2^-$-positive cells shows that **3b** also causes statistically significant accumulation of $^{\bullet}O_2^-$ in mitochondria (Fig. 4D). Current result reports on the ability of **3b** to induce such overwhelming flow of $^{\bullet}O_2^-$ production that mitochondrial (manganese) superoxide dismutase (SOD2) cannot effectively convert to hydrogen peroxide. Here discovered feature of **3b** to extensively promote formation of reactive oxygen species (ROS) can explain more vigorous activity of this compound compared to **2a**, while further discussion regarding possible intracellular interactions of **3b** that underlie its pro-oxidative activity is beyond the scope of the current investigation. However, it remains unclear why the treatment with **3b** did not achieve the same impact on other cell lines (Table S1), especially knowing that LoVo and MCF-7 are phenotypes with low SOD2 expression and/or activity and can be expected of them to be at least equally or even more vulnerable than A549 (Piotrowska et al., 2013). Further studies are required to demonstrate which mitochondrial electron carrier interacts with **3b**, as well as whether this compound undergoes intracellular transformation that yields product with more powerful pro-oxidant features in A549 cells than in other here tested malignant models.

Apart from pro-apoptotic activity, anticancer drugs can also target other processes important for tumor growth and survival. Here we investigated the impact of compounds **2a** and **3b** on cell migration as an important mechanism in the formation of distant metastasis (Paul et al., 2017). Both compounds have been tested at low concentrations that cause minor induction of apoptosis (Fig. 3A), which allows observation whether our molecules can produce beneficial effect beyond arousing cell death. Basal migration of A549 cells is inhibited by both compounds, while **2a** scored statistically significant suppression of cellular motility in both tested concentrations (Fig. 4E and 4F). In the current investigation was not examined which particular step in complex metastatic cascade is regulated by **2a**, and further study is needed to appoint the course of its antimigratory activity.

The main goal in anticancer drug discovery and development is to introduce therapy that would specifically target malignant cells while sparing healthy tissues. Anticancer drugs that are in clinical use, including modern targeted therapies, can induce various side effects (Kroschinsky et al., 2017). Toxicological profile of a new drug can be specified through a panel of *in vivo* tests and clinical trials, while a full spectrum of probable adverse reactions is impossible to predict in early phases of laboratory investigation. Therefore, selection of an appropriate experimental model to study potential side effects of a newly synthesized drug is hard to make. However, cutaneous lesions are frequently described in malignant patients treated with either conventional or targeted therapeutics, while underlying mechanisms are assumed to be variable and still poorly understood (Ng et al., 2018). Those data served as a rational to use human keratinocytes (HaCaT cells) as the model for assessment of **2a** and **3b** toxicity. As is presented in Figures S45-S47 and Table S1, cell survival in HaCaT samples subjected to **2a** exceeds that in A549 samples. Thus, percentages of HaCaT live cells treated with **2a** at 100, 75, 50, and 30 μM are 61 ± 5 %, 66 ± 1 %, 78 ± 9 %, and 82 ± 5 %, respectively, which clearly indicate that keratinocytes are less sensitive to activity of **2a** compared to A549 cells (Figures S45 and S47). On the contrary, compound **3b** demonstrates vigorous activity on HaCaT cells, with 14 ± 2 %, 13 ± 2 %, 25 ± 1 % and 78 ± 14 % cell survival in samples treated at 100, 75, 50 and 30 μM, respectively (Figures S46 and S47). These data demonstrate that **2a** was revealed a certain degree of selectivity toward malignant cells, while it can be expected of **3b** to induce notable cutaneous side effects after its application to men. Moreover, we also evaluated hepatotoxic potentials of **2a** and **3b**, and **3b** is the only that induced HepG-2 cell death in 10 ± 2 %, 12 ± 6 %, 22 ± 6 %, and 29 ± 1 % at 30, 50, 75 and 100 μM, respectively (Figures S48 and S49).

3.4.1. Plausible anticancer targets suggested by pharmacophoric similarity search

Pharmacophoric similarity proved to be a valuable tool for target identification of small molecules, especially when integrated into network pharmacology protocols (Bahuguna et al., 2019; Jiang et al., 2020; Shi et al., 2020). In this study, target fishing was performed using PharmMapper web server.

Fig. 4 Profiles of **2a** and **3b** anticancer activity on A549 cells. (A) Representative images of cell cycle distribution after 12 h of treatment. Data included are the mean ± SD percentages of cells at the G0/G1, S, and G2/M phases, as the result of two replicates from independent experiments. (B) Percentages of cells positive for activated caspase-8, −9, or both in non-treated samples (closed bars) and after 6 h of treatment with investigated compounds at 50 μM (open bars). The statistical evaluation has been performed using unpaired *t*-test with Welch's correction comparing treated to non-treated populations. (C) Representative histograms of cells stained with MitoSOX Red dye performed after 6 h treatment with investigated compounds at 50 μM, with the mean ± SD percentages of cells positive for superoxide ($^{\bullet}O_2^-$) production calculated from data of three independent replicates. (D) Mean fluorescence intensity (MFI) expressed in arbitrary units [AU], computed for $^{\bullet}O_2^-$-positive subpopulation from data of three independent replicates. Statistical significance was computed using the Kruskal-Wallis test with unpaired *t*-test with Welch's correction as post-test. (E) Representative images of scratch assay acquired by Celigo imaging cytometer after cells were stained with Calcein AM. Images were taken just before the addition of compounds (Day 0) and 24 h later (Day 1). (F) Mean ± SD plot of open wound area after treatment with investigated compounds, determined by TScratch software analysis of images acquired at 0 and 24 h. Statistical significance was tested using the Kruskal-Wallis test and unpaired *t*-test with Welch's correction.

Table 4 Protein targets identified through pharmacophore matching between PharmMapper database and compounds **2a** and **3b**.

Cp.	Target	PDB code	Fit Score	Norm. Fit score	Z' score	Relation to cancer
2a	Collagenase-2	1JAP	3.466	0.693	2.734	Upregulated in many different tumors (Van Lint and Libert, 2006)
	Abl-1 kinase	2HZI	3.860	0.482	2.574	Chronic myelogenous leukaemia (Shah et al., 2007)
	Proto-oncogene serine/threonine-protein kinase Pim-1	2OBJ	2.955	0.985	1.159	Associated with lung adenocarcinoma through potentiation of c-MET pathway (Cao et al., 2018)
	Caspase-3	3DEJ	2.922	0.974	1.053	Activation related to DNA damage and apoptosis in A549 cells (Lin et al., 2008)
	Complement C1r subcomponent	1GPZ	2.904	0.726	1.036	Overexpressed in ovary adenocarcinoma (Lin et al., 2004)
3b	Dipeptidyl peptidase 4 (DPPH4)	1ORW	3.822	0.637	3.339	Tumor suppressor or activator (Bishnoi et al., 2019)
	Baculoviral IAP repeat-containing protein 4	3HL5	3.662	0.6104	2.922	Supresses apoptosis through inhibition of caspases (Qin et al., 2012)
	Collagenase-2	1JAP	3.528	0.706	2.755	Upregulated in many different tumors (Van Lint and Libert, 2006)
	Tyrosine-protein phosphatase non-receptor type 1 (PTP1B)	1NWE	3.361	0.726	2.524	Dephosphorylation of specific substrates leading to tumor suppression or tumor promotion(Lessard et al., 2010)

Several molecular targets relevant for anticancer activity are identified and their relevance was confirmed in literature (Table 4). The pharmacophore matching between **2a**, **3b**, and several cancer-related protein targets is shown in ESI, Figures S50 and S51.

Targets with high values of normalized FitScore and particularly with high positive z' values are rational guesses for further structure-based computational studies and experimental validation. Matrix metalloproteinase-8, proto-oncogene serine/threonine-protein kinase Pim-1 and tyrosine-protein phosphatase non-receptor type 1 (PTP1B) are plausible molecular targets for this class of anticancer agents.

The suggested anticancer targets are a good starting point for further target deconvolution studies that would include enzymatic, genomics, and cell-based assays.

4. Conclusion

A series of twelve novel cinnamic acid hydrazides structurally related to isoniazid and anticancer agents 5-HP and 3-AP was synthesized from four MTCHs and three cinnamic acid derivatives using a simple coupling strategy via acid chlorides. ^{1}H NMR and 2D NOESY spectra indicate that the (*E*,*E*)-isomer is a dominant form of cinnamic acid hydrazides in a solution. All twelve compounds obey RO5, show moderate aqueous solubility and poor BBB permeability. Evaluation of ADME properties indicated high permeability and good absorption through the human intestine for the majority of the compounds.

Over the course of this study, we examined our compounds on two distinctive biological models. Each of those models is related with different type of disease, regarding etiology and treatment options. Here presented results of preliminary investigation on biological activity provide evidences that potentially effective and safe drugs against TB and lung cancer can be found within this relatively small series of new chemicals. Structurally, treated *Mtb* strains were more sensitive to compounds with no chlorine added to phenyl ring, while A549 cells showed better response to treatment with chlorine analogues of core structures. Compound **3** is the only one with ability to reduce survival of *Mtb* bacilli for 90 % in all three strains, had been achieved neither by INH nor RIF. More importantly, none of four compounds that gained MIC on any of *Mtb* strains did induce death in HepG-2 cells, which is highly promising considering hepatotoxicity is a serious problem of the current anti-TB therapies. On the contrary, compounds **2a** and **3b**, both strong inducers of apoptotic death in A549 cells, revealed not to have equivalent toxicological profiles. While **2a** induced mild acute skin toxicity in HaCaT cells and had no effect on survival of HepG-2 cells, **3b** significantly impacted vitality of cells in each tested model. Although both compounds demonstrated to interfere with DNA replication process according to changes in distribution of A549 cells during mitotic division, and both of them initiated apoptosis over the activation of caspase-9, **3b** was showed as a potent inducer of mitochondrial $^{\bullet}O_2^-$ production, whereas **2a** did not. Thus, capacity of **3b** to cause ROS generation within treated cells may be the reason for its non-selective activity toward cancer cells. Additionally, compound **2a** significantly inhibited migratory activity of A549 cells while **3b** was ineffective. Target fishing study based on pharmacophoric similarity indicates that Collagenase-2, Pim-1 kinase, and protein-tyrosine phosphatase 1B (PTP1B) are plausible anticancer targets of these two compounds. Advantageous penetration ability through *Mtb* cell wall and interruption of the iron pool of treated bacilli are excluded as mechanisms responsible for superior anti-*Mtb* activity of **3** over other compounds. The overall conclusion of this study is that compounds **3** and **2a** deserve further experimental and *in silico* investigations regarding mechanisms of their anti-*Mtb* and anti-cancer activity, respectively.

Funding

This research was supported by the Ministry of Education, Science and Technological Development of the Republic of Serbia, GRANT No 451–03-9/2021–14/200110, 451–03-9/2021–14/200043, 451–03-9/2021–14/200168, 451–03-9/2021–14/200135, and by the Science Fund of the Republic of Serbia, PROMIS, #GRANT No 6059147, IN-DEPTH.

Declaration of Competing Interest

The authors declare that they have no known competing financial interests or personal relationships that could have appeared to influence the work reported in this paper.

Appendix A. Supplementary material

Supplementary data to this article can be found online at https://doi.org/10.1016/j.arabjc.2021.103532.

References

Abu El-Reash, G.M., El-Gammal, O.A., Radwan, A.H., 2014. Molecular structure and biological studies on Cr(III), Mn(II) and Fe(III) complexes of heterocyclic carbohydrazone ligand. Spectrochim. Acta A. 121, 259–267. https://doi.org/10.1016/j.saa.2013.10.048.

Alahari, A., Trivelli, X., Gu + ¬rardel, Y., Dover, L.G., Besra, G.S., Sacchettini, J.C., Reynolds, R.C., Coxon, G.D., Kremer, L., 2007. Thiacetazone, an Antitubercular Drug that Inhibits Cyclopropanation of Cell Wall Mycolic Acids in Mycobacteria. PLOS ONE. 2,. https://doi.org/10.1371/journal.pone.0001343 e1343.

Almeida Da Silva, P.E., Palomino, J.C., 2011. Molecular basis and mechanisms of drug resistance in Mycobacterium tuberculosis: classical and new drugs. J. Antimicrob. Chemother. 66, 1417–1430. https://doi.org/10.1093/jac/dkr173.

Bahuguna, A., Singh, A., Kumar, P., Dhasmana, D., Krishnan, V., Garg, N., 2019. Bisindolemethane derivatives as highly potent anticancer agents: Synthesis, medicinal activity evaluation, cell-based compound discovery, and computational target predictions. Comput. Biol. Med. 116,. https://doi.org/10.1016/j.compbiomed.2019.103574 103574.

Bishnoi, R., Hong, Y.R., Shah, C., Ali, A., Skelton, W., Huo, J., Dang, N., Dang, L., 2019. Dipeptidyl peptidase 4 inhibitors as novel agents in improving survival in diabetic patients with colorectal cancer and lung cancer: A Surveillance Epidemiology and Endpoint Research Medicare study. Cancer Med. 8, 3918–3927. https://doi.org/10.1002/cam4.2278.

Bonaccorso, C., Marzo, T., La, M.D., 2019. Biological Applications of Thiocarbohydrazones and Their Metal Complexes: A Perspective Review. Pharmaceuticals (Basel). 13, 4–22. https://doi.org/10.3390/ph13010004.

Bozic, A., Marinkovic, A., Bjelogrlic, S., Todorovic, T.R., Cvijetic, I. N., Novakovic, I., Muller, C.D., Filipovic, N.R., 2016. Quinoline based mono- and bis-(thio)carbohydrazones: synthesis, anticancer activity in 2D and 3D cancer and cancer stem cell models. RSC Adv. 6, 104763–104781. https://doi.org/10.1039/C6RA23940D.

Bozic, A.R., Bjelogrlic, S.K., Novakovic, I.T., Filipovic, N.R., Petrovic, P.M., Marinkovic, A.D., Todorovic, T.R., Cvijetic, I. N., 2018. Antimicrobial Activity of Thiocarbohydrazones: Experimental Studies and Alignment-Independent 3D QSAR Models. ChemistrySelect. 3, 2215–2221. https://doi.org/10.1002/slct.201702691.

Cao, L., Wang, F., Li, S., Wang, X., Huang, D., Jiang, R., 2018. PIM1 kinase promotes cell proliferation, metastasis and tumor growth of lung adenocarcinoma by potentiating the c-MET signaling pathway. Cancer Lett. 444, 116–126. https://doi.org/10.1016/j.canlet.2018.12.015.

Castelo-Branco, F.S., de Lima, E.C., Domingos, J.L.D.O., Pinto, A. C., Louren + şo, M.C., Gomes, K.M., Costa-Lima, M.M., Araujo-Lima, C.F., Aiub, C.A.F., Felzenszwalb, I., Costa, T.E., Penido, C., Henriques, M.G., Boechat, N., 2018. New hydrazides derivatives of isoniazid against Mycobacterium tuberculosis: Higher potency and lower hepatocytotoxicity. Eur. J. Med. Chem. 146, 529–540. https://doi.org/10.1016/j.ejmech.2018.01.071.

Chao, J., Synold, T.W., Morgan, R.J., Kunos, C., Longmate, J., Lenz, H.J., Lim, D., Shibata, S., Chung, V., Stoller, R.G., Belani, C.P., Gandara, D.R., McNamara, M., Gitlitz, B.J., Lau, D.H., Ramalingam, S.S., Davies, A., Espinoza-Delgado, I., Newman, E.M., Yen, Y., 2012. A phase I and pharmacokinetic study of oral 3-aminopyridine-2-carboxaldehyde thiosemicarbazone (3-AP, NSC #663249) in the treatment of advanced-stage solid cancers: a California Cancer Consortium Study. Cancer Chemother. Pharmacol. 69, 835–843. https://doi.org/10.1007/s00280-011-1779-5.

Dagenais, G.R., Leong, D.P., Rangarajan, S., Lanas, F., Lopez-Jaramillo, P., Gupta, R., Diaz, R., Avezum, A., Oliveira, G.B.F., Wielgosz, A., Parambath, S.R., Mony, P., Alhabib, K.F., Temizhan, A., Ismail, N., Chifamba, J., Yeates, K., Khatib, R., Rahman, O., Zatonska, K., Kazmi, K., Wei, L., Zhu, J., Rosengren, A., Vijayakumar, K., Kaur, M., Mohan, V., Yusufali, A., Kelishadi, R., Teo, K.K., Joseph, P., Yusuf, S., 2020. Variations in common diseases, hospital admissions, and deaths in middle-aged adults in 21 countries from five continents (PURE): a prospective cohort study. Lancet. 395, 785–794. https://doi.org/10.1016/S0140-6736(19)32007-0.

Daina, A., Michielin, O., Zoete, V., 2017. SwissADME: a free web tool to evaluate pharmacokinetics, drug-likeness and medicinal chemistry friendliness of small molecules. Sci. Rep. 7, 42717–42729. https://doi.org/10.1038/srep42717.

Dalberto, P.F., de Souza, E.V., Abbadi, B.L., Neves, C.E., Rambo, R. S., Ramos, A.S., Macchi, F.S., Machado, P., Bizarro, C.V., Basso, L.A., 2020. Handling the Hurdles on the Way to Anti-tuberculosis Drug Development. Front. Chem. 8,. https://doi.org/10.3389/fchem.2020.586294 586294.

Danchuk, S., Mcintosh, F., Jamieson, F., May, K., Behr, M., 2019. BCG strains with defined resistance mutations: a new tool for TB lab quality control. Clin. Microbiol. Infect. 26, 384.e5–384.e8. https://doi.org/10.1016/j.cmi.2019.10.033.

De, P., Baltas, M., Belval, F., 2011a. Cinnamic Acid Derivatives as Anticancer Agents-A Review. Curr. Med. Chem. 18, 1672–1703. https://doi.org/10.2174/092986711795471347.

De, P., Belval, F., Bacque, C., Baltas, M., 2012. Cinnamic Acid Derivatives in Tuberculosis, Malaria and Cardiovascular Diseases - A Review. Curr. Org. Chem. 16, 747–768. https://doi.org/10.2174/138527212799958020.

De, P., Koumba Yoya, G., Constant, P., Bedos-Belval, F., Duran, H., Saffon, N., Daffe, M., Baltas, M., 2011b. Design, Synthesis, and Biological Evaluation of New Cinnamic Derivatives as Antituberculosis Agents. J. Med. Chem. 54, 1449–1461. https://doi.org/10.1021/jm101510d.

DeConti, R.C., Toftness, B.R., Agrawal, K.C., Tomchick, R., Mead, J.A.R., Bertino, J.R., Sartorelli, A.C., Creasey, W.A., 1972. Clinical and Pharmacological Studies with 5-Hydroxy-2-formylpyridine Thiosemicarbazone. Cancer Res. 32, 1455–1462 http://cancerres.aacrjournals.org/content/32/7/1455.abstract.

Dias, K.S., de Paula, C.T., dos Santos, T., Souza, I.N.O., Boni, M.S., Guimar + úes, M.J.R., da Silva, F.M.R., Castro, N.G., Neves, G. A., Veloso, C.C., Coelho, M.M., de Melo, I.S., Giusti, F.C.V., Giusti-Paiva, A., da Silva, M.L., Dardenne, L.E., Guedes, I.A., Pruccoli, L., Morroni, F., Tarozzi, A., Viegas, C., 2017. Design, synthesis and evaluation of novel feruloyl-donepezil hybrids as potential multitarget drugs for the treatment of Alzheimer's disease. Eur. J. Med. Chem. 130, 440–457. https://doi.org/10.1016/j.ejmech.2017.02.043.

Dragset, M.S., Poce, G., Alfonso, S., Padilla-Benavides, T., Ioerger, T. R., Kaneko, T., Sacchettini, J.C., Biava, M., Parish, T., Arguello, J. M., Steigedal, M., Rubin, E.J., 2015. A Novel Antimycobacterial Compound Acts as an Intracellular Iron Chelator. Antimicrob. Agents Chemother. 59, 2256–2264. https://doi.org/10.1128/AAC.05114-14.

En, Z., Wang, M.M., Huang, S.C., Xu, S.M., Cui, D.Y., Bo, Y.L., Bai, P.Y., Hua, Y.G., Xiao, C.L., Qin, S., 2017. NOTA Analogue: a First Dithiocarbamate Inhibitor of Metallo-beta-lactamases.

Bioorg. Med. Chem. Lett. 28, 214–221. https://doi.org/10.1016/j.bmcl.2017.10.074.

Fernandes, G.F.D.S., Salgado, H.R.N., Santos, J.L.D., 2017. Isoniazid: A Review of Characteristics, Properties and Analytical Methods. Crit. Rev. Anal. Chem. 47, 298–308. https://doi.org/10.1080/10408347.2017.1281098.

Feun, L., Modiano, M., Lee, K., Mao, J., Marini, A., Savaraj, N., Plezia, P., Almassian, B., Colacino, E., Fischer, J., MacDonald, S., 2002. Phase I and pharmacokinetic study of 3-aminopyridine-2-carboxaldehyde thiosemicarbazone (3-AP) using a single intravenous dose schedule. Cancer Chemother. Pharmacol. 50, 223–229. https://doi.org/10.1007/s00280-002-0480-0.

Gaikwad, N., Nanduri, S., Madhavi, Y.V., 2019. Cinnamamide: An insight into the pharmacological advances and structure–activity relationships. Eur. J. Med. Chem. 181, 111561–111584. https://doi.org/10.1016/j.ejmech.2019.07.064.

Glaziou, P., 2020. Predicted impact of the COVID-19 pandemic on global tuberculosis deaths in 2020, medRxiv. 2020. https://doi.org/10.1101/2020.04.28.20079582.

Global Burden of Disease Cancer Collaboration, 2019. Global, Regional, and National Cancer Incidence, Mortality, Years of Life Lost, Years Lived With Disability, and Disability-Adjusted Life-Years for 29 Cancer Groups, 1990 to 2017: A Systematic Analysis for the Global Burden of Disease Study, JAMA Oncol. 5, 1749-1768. https://doi.org/10.1001/jamaoncol.2019.2996.

Guzman, J.D., 2014. Natural cinnamic acids, synthetic derivatives and hybrids with antimicrobial activity. Molecules. 19, 19292–19349. https://doi.org/10.3390/molecules191219292.

Haj Mohammad Ebrahim Tehrani, K., Kobarfard, F., Azerang, P., Mehravar, M., Soleimani, Z., Ghavami, G., Sardari, S., 2013. Synthesis and Antimycobacterial Activity of Symmetric Thiocarbohydrazone Derivatives against Mycobacterium bovis BCG. Iran. J. Pharm. Res. 12, 331–346 https://pubmed.ncbi.nlm.nih.gov/24250608.

Heffeter, P., Pape, V.F.S., Enyedy, A., Keppler, B.K., Szakacs, G., Kowol, C.R., 2018. Anticancer Thiosemicarbazones: Chemical Properties, Interaction with Iron Metabolism, and Resistance Development. Antioxidants & Redox Signaling. 30, 1062–1082. https://doi.org/10.1089/ars.2017.7487.

Hofmann-Thiel, S., Hoffmann, H., Hillemann, D., Rigouts, L., Deun, A., Kranzer, K., 2017. How should discordance between molecular & growth-based assays for rifampicin resistance be investigated? Int. J. Tuberc. Lung Dis. 21, 721–726. https://doi.org/10.5588/ijtld.17.0140.

Hruskova, K., Potuckova, E., Hergeselova, T., Liptakova, L., Haskova, P., Mingas, P., Kovarikova, P., Simunek, T., Vavrova, K., 2016. Aroylhydrazone iron chelators: Tuning antioxidant and antiproliferative properties by hydrazide modifications. Eur. J. Med. Chem. 120, 97–110. https://doi.org/10.1016/j.ejmech.2016.05.015.

Jiang, L., Lu, J., Qin, Y., Jiang, W., Wang, Y., 2020. Antitumor effect of guava leaves on lung cancer: A network pharmacology study. Arab. J. Chem. 13, 7773–7797. https://doi.org/10.1016/j.arabjc.2020.09.010.

Jo, K.W., Yeo, Y., Sung, H., Kim, M.N., Shim, T.S., 2017. Analysis of discrepant results between the Genotype MTBDRplus assay and an antimicrobial drug susceptibility test for isoniazid-resistant tuberculosis. Respir. Med. 122, 12–17. https://doi.org/10.1016/j.rmed.2016.11.016.

Kakwani, M.D., Suryavanshi, P., Ray, M., Rajan, M.G.R., Majee, S., Samad, A., Devarajan, P., Degani, M.S., 2011. Design, synthesis and antimycobacterial activity of cinnamide derivatives: A molecular hybridization approach. Bioorg. Med. Chem. Lett. 21, 1997–1999. https://doi.org/10.1016/j.bmcl.2011.02.022.

Kang, J.Y., Hur, J., Kim, S., Jeon, S., Lee, J., Kim, Y.J., Kim, S.C., Park, Y.J., Kim, Y.K., Moon, H.S., 2019. Clinical implications of discrepant results between genotypic MTBDR plus and phenotypic Lowenstein-Jensen method for isoniazid or rifampicin drug susceptibility tests in tuberculosis patients. J. Thorac. Dis. 11, 400–409. https://doi.org/10.21037/jtd.2019.01.58.

Kroschinsky, F., Stolzel, F., von Bonin, S., Beutel, G., Kochanek, M., Kiehl, M., Schellongowski, P.,on behalf of the Intensive Care in Hematological and Oncological Patients (iCHOP) Collaborative Group, 2017. New drugs, new toxicities: severe side effects of modern targeted and immunotherapy of cancer and their management, Crit. Care. 21, 89-99. https://doi.org/10.1186/s13054-017-1678-1.

Kumari, V., Bharathi, K., Prabhu, K., Ponnudurai, K., 2016. Synthesis and Biological Evaluation of N-Cinnamoyl and Mandelate Metformin Analogues, Asian. J. Chem. 28, 1895–1898. https://doi.org/10.14233/ajchem.2016.19633.

Lessard, L., Stuible, M., Tremblay, M.L., 2010. The two faces of PTP1B in cancer. Biochim. Biophys. Acta (BBA) - Proteins Proteom. 1804, 613–619. https://doi.org/10.1016/j.bbapap.2009.09.018.

Li, Z.J., Cai, L., Mei, R.F., Dong, J.W., Li, S.Q., Yang, X.Q., Zhou, H., Yin, T.P., Ding, Z.T., 2015. A highly efficient transformation of cis- to trans-cinnamic acid derivatives by iodine. Tetrahedron Lett. 56, 7197–7200. https://doi.org/10.1016/j.tetlet.2015.11.050.

Lin, N., Liu, S., Li, N., Wu, P., An, H., Yu, Y., Wan, T., Cao, X., 2004. A novel human dendritic cell-derived C1r-like serine protease analog inhibits complement-mediated cytotoxicity. Biochem. Biophys. Res. Commun. 321, 329–336. https://doi.org/10.1016/j.bbrc.2004.06.127.

Lin, S.S., Huang, H.P., Yang, J.S., Wu, J.Y., Hsai, T.C., Lin, C.C., Lin, C.W., Kuo, C.L., Gibson Wood, W., Chung, J.G., 2008. DNA damage and endoplasmic reticulum stress mediated curcumin-induced cell cycle arrest and apoptosis in human lung carcinoma A-549 cells through the activation caspases cascade- and mitochondrial-dependent pathway. Cancer Lett. 272, 77–90. https://doi.org/10.1016/j.canlet.2008.06.031.

Lipinski, C.A., Lombardo, F., Dominy, B.W., Feeney, P.J., 2001. Experimental and computational approaches to estimate solubility and permeability in drug discovery and development settings1PII of original article: S0169–409X(96), 00423–1. The article was originally published in Advanced Drug Delivery Reviews 23 (1997) 3–25. Adv. Drug Deliv. Rev. 46, 3–26. https://doi.org/10.1016/S0169-409X(00)00129-0.

Luo, Y., Zhu, Y., Ran, K., Liu, Z., Wang, N., Feng, Q., Zeng, J., Zhang, L., He, B., Ye, T., Zhu, S., Qiu, X., Yu, L., 2015. Synthesis and biological evaluation of N-(4-phenylthiazol-2-yl)cinnamamide derivatives as novel potential anti-tumor agents. Med. Chem. Commun. 6, 1036–1042. https://doi.org/10.1016/j.ejmech.2019.07.064.

Ma, B., Goh, B., Tan, E., Lam, K., Soo, R., Leong, S., Wang, L., Mo, F., Chan, A., Zee, B., Mok, T., 2008. A multicenter phase II trial of 3-aminopyridine-2-carboxaldehyde thiosemicarbazone (3-AP, Triapine) and gemcitabine in advanced non-small-cell lung cancer with pharmacokinetic evaluation using peripheral blood mononuclear cells. Invest. New Drugs. 26, 169–173. https://doi.org/10.1007/s10637-007-9085-0.

Maitra, A., Munshi, T., Healy, J., Martin, L.T., Vollmer, W., Keep, N. H., Bhakta, S., 2019. Cell wall peptidoglycan in Mycobacterium tuberculosis: An Achilles' heel for the TB-causing pathogen. FEMS Microbiol. Rev. 43, 548–575. https://doi.org/10.1093/femsre/fuz016.

Matsuhira, T., Yamamoto, H., Okamura, T.A., Ueyama, N., 2008. Manipulation of an intramolecular NHΓd'»O hydrogen bond by photoswitching between stable E/Z isomers of the cinnamate framework. Org. Biomol. Chem. 6, 1926–1933. https://doi.org/10.1039/b719960k.

Miller, A.B., Fox, W., Tall, R., 1966. An international co-operative investigation into thiacetazone (thioacetazone) side-effects. Tubercle. 47, 33–74. https://doi.org/10.1016/S0041-3879(66)80051-X.

Momidi, B.K., Tekuri, V., Trivedi, D.R., 2017. Multi-signaling thiocarbohydrazide based colorimetric sensors for the selective

recognition of heavy metal ions in an aqueous medium. Spectrochim. Acta A Mol. Biomol. Spectrosc. 180, 175–182. https://doi.org/10.1016/j.saa.2017.03.010.

Murad, H., Hawat, M., Ekhtiar, A., AlJapawe, A., Abbas, A., Darwish, H., Sbenati, O., Ghannam, A., 2016. Induction of G1-phase cell cycle arrest and apoptosis pathway in MDA-MB-231 human breast cancer cells by sulfated polysaccharide extracted from Laurencia papillosa. Cancer Cell Int. 16, 39–49. https://doi.org/10.1186/s12935-016-0315-4.

Ng, C.Y., Chen, C.B., Wu, M.Y., Wu, J., Yang, C.H., Hui, R.C., Chang, Y.C., Lu, C.W., 2018. Anticancer Drugs Induced Severe Adverse Cutaneous Drug Reactions: An Updated Review on the Risks Associated with Anticancer Targeted Therapy or Immunotherapies. J. Immunol. Res. 2018, 5376476. https://doi.org/10.1155/2018/5376476.

Nunn, P., Porter, J., Winstanley, P., 1993. Thiacetazone–avoid like poison or use with care? Trans. R. Soc. of Trop. Med. Hyg. 87, 578–582. https://doi.org/10.1016/0035-9203(93)90096-9.

Paul, C.D., Mistriotis, P., Konstantopoulos, K., 2017. Cancer cell motility: lessons from migration in confined spaces. Nat. Rev. Cancer. 17, 131–140. https://doi.org/10.1038/nrc.2016.123.

Piotrowska, H., Kucinska, M., Murias, M., 2013. Expression of CYP1A1, CYP1B1 and MnSOD in a panel of human cancer cell lines. Mol. Cell. Biochem. 383, 95–102. https://doi.org/10.1007/s11010-013-1758-8.

Pires, D.E.V., Blundell, T.L., Ascher, D.B., 2015. pkCSM: Predicting Small-Molecule Pharmacokinetic and Toxicity Properties Using Graph-Based Signatures. J. Med. Chem. 58, 4066–4072. https://doi.org/10.1021/acs.jmedchem.5b00104.

Pontiki, E., Hadjipavlou-Litina, D., Litinas, K., Geromichalos, G., 2014. Novel cinnamic acid derivatives as antioxidant and anticancer agents: design, synthesis and modeling studies. Molecules. 19, 9655–9674. https://doi.org/10.3390/molecules19079655.

Qin, S., Yang, C., Li, S., Xu, C., Zhao, Y., Ren, H., 2012. Smac: Its role in apoptosis induction and use in lung cancer diagnosis and treatment. Cancer Lett. 318, 9–13. https://doi.org/10.1016/j.canlet.2011.12.024.

Sankara Rao, N., Nagesh, N., Lakshma Nayak, V., Sunkari, S., Tokala, R., Kiranmai, G., Regur, P., Shankaraiah, N., Kamal, A., 2019. Design and synthesis of DNA-intercalative naphthalimide-benzothiazole/cinnamide derivatives: cytotoxicity evaluation and topoisomerase-II inhibition. Med. Chem. Commun. 10, 72–79. https://doi.org/10.1016/j.ejmech.2019.07.064.

Seifert, M., Catanzaro, D., Catanzaro, A., Rodwell, T.C., 2015. Genetic Mutations Associated with Isoniazid Resistance in Mycobacterium tuberculosis: A Systematic Review. PLOS ONE. 10,. https://doi.org/10.1371/journal.pone.0119628 e0119628.

Shah, N., Skaggs, B., Branford, S., Hughes, T., Nicoll, J., Paquette, R., Sawyers, C., 2007. Sequential ABL kinase inhibitor therapy selects for compound drug-resistant BCR-ABL mutations with altered oncogenic potency. J. Clin. Invest. 117, 2562–2569. https://doi.org/10.1172/JCI30890.

Shi, H., Xie, D., Yang, R., Cheng, Y., 2014. Synthesis of Caffeic Acid Phenethyl Ester Derivatives, and Their Cytoprotective and Neurite-togenic Activities in PC12 Cells. J. Agric. Food Chem. 62, 5046–5053. https://doi.org/10.1021/jf500464k.

Shi, P., Xie, Y., Xie, R., Lin, Z., Yao, H., Wu, S., 2020. An Integrated Pharmacokinetic Study of an Acanthopanax senticosus Extract Preparation by Combination of Virtual Screening, Systems Pharmacology, and Multi-Component Pharmacokinetics in Rats. Front. Pharmacol. 11, 1295. https://doi.org/10.3389/fphar.2020.01295.

Shuab, R., Lone, R., Koul, K.K., 2016. Cinnamate and cinnamate derivatives in plants. Acta Physiol. Plant. 38, 64–72. https://doi.org/10.1007/s11738-016-2076-z.

Sova, M., 2012. Antioxidant and Antimicrobial Activities of Cinnamic Acid Derivatives. Mini Rev. Med. Chem. 12, 749–767. https://doi.org/10.2174/138955712801264792.

Teixeira, C., Vale, N., Perez, B., Gomes, A., Gomes, J.R.B., Gomes, P., 2014. Recycling Classical Drugs for Malaria. Chem. Rev. 114, 11164–11220. https://doi.org/10.1021/cr500123g.

Teixeira, C., Ventura, C., Gomes, J.R.B., Gomes, P., Martins, F., 2020. Cinnamic Derivatives as Antitubercular Agents: Characterization by Quantitative Structure-Activity Relationship Studies. Molecules. 25, 456–466. https://doi.org/10.3390/molecules25030456.

Trotsko, N., Golus, J., Kazimierczak, P., Paneth, A., Przekora, A., Ginalska, G., Wujec, M., 2020. Design, synthesis and antimycobacterial activity of thiazolidine-2,4-dione-based thiosemicarbazone derivatives. Bioorg. Chem. 97, 103676–103684. https://doi.org/10.1016/j.bioorg.2020.103676.

Van Lint, P., Libert, C., 2006. Matrix metalloproteinase-8: Cleavage can be decisive. Cytokine Growth Factor Rev. 17, 217–223. https://doi.org/10.1016/j.cytogfr.2006.04.001.

Van Summeren, A., Renes, J., Bouwman, F.G., Noben, J.P., van Delft, J.H.M., Kleinjans, J.C.S., Mariman, E.C.M., 2010. Proteomics Investigations of Drug-Induced Hepatotoxicity in HepG2 Cells. Toxicol. Sci. 120, 109–122. https://doi.org/10.1093/toxsci/kfq380.

Wang, P., Pradhan, K., Zhong, X.B., Ma, X., 2016. Isoniazid metabolism and hepatotoxicity. Acta Pharm. Sin. B. 6, 384–392. https://doi.org/10.1016/j.apsb.2016.07.014.

World Health Organization, 2021. World Health Organization Global Health Observatory (GHO) data. https://www.who.int/gho/tb/epidemic/cases_deaths/en/ (accessed February 10, 2021).

Yen, Y., Margolin, K., Doroshow, J., Fishman, M., Johnson, B., Clairmont, C., Sullivan, D., Sznol, M., 2004. A phase I trial of 3-aminopyridine-2-carboxaldehyde thiosemicarbazone in combination with gemcitabine for patients with advanced cancer. Cancer Chem. Pharmacol. 54, 331–342. https://doi.org/10.1007/s00280-004-0821-2.

Zhang, J.H., Xu, M., 2000. DNA fragmentation in apoptosis. Cell Res. 10, 205–211. https://doi.org/10.1038/sj.cr.7290049.

Zhu, B., Shang, B., Li, Y., Zhen, Y., 2016. Inhibition of histone deacetylases by trans-cinnamic acid and its antitumor effect against colon cancer xenografts in athymic mice. Mol. Med. Rep. 13, 4159–4166. https://doi.org/10.3892/mmr.2016.5041.